



HAL
open science

Cumulative right-lateral fault slip rate across the Zagros-Makran transfer zone: role of the Minab-Zendan fault system in accommodating Arabia-Eurasia convergence in southeast Iran

V. Regard, O Bellier, J.-C. Thomas, D. Bourles, Sébastien Bonnet, M. R. Abbassi, Regis Braucher, J. Mercier, E. Shabanian, Sh. Soleymani, et al.

► To cite this version:

V. Regard, O Bellier, J.-C. Thomas, D. Bourles, Sébastien Bonnet, et al.. Cumulative right-lateral fault slip rate across the Zagros-Makran transfer zone: role of the Minab-Zendan fault system in accommodating Arabia-Eurasia convergence in southeast Iran. *Geophysical Journal International*, 2005, 162 (1), pp.177-203. 10.1111/J.1365-246X.2005.02558.X . hal-00321123

HAL Id: hal-00321123

<https://hal.science/hal-00321123>

Submitted on 6 Jul 2017

HAL is a multi-disciplinary open access archive for the deposit and dissemination of scientific research documents, whether they are published or not. The documents may come from teaching and research institutions in France or abroad, or from public or private research centers.

L'archive ouverte pluridisciplinaire **HAL**, est destinée au dépôt et à la diffusion de documents scientifiques de niveau recherche, publiés ou non, émanant des établissements d'enseignement et de recherche français ou étrangers, des laboratoires publics ou privés.

Cumulative right-lateral fault slip rate across the Zagros–Makran transfer zone: role of the Minab–Zendan fault system in accommodating Arabia–Eurasia convergence in southeast Iran

V. Regard,^{1,*} O. Bellier,¹ J.-C. Thomas,² D. Bourlès,¹ S. Bonnet,³ M. R. Abbassi,⁴ R. Braucher,¹ J. Mercier,⁵ E. Shabanian,⁴ Sh. Soleymani⁴ and Kh. Feghhi⁴

¹Centre Européen de Recherche et d'Enseignement en Géosciences de l'Environnement (CEREGE), UMR CNRS 6635, University P. Cézanne Aix-Marseille III, France

²Laboratoire de Géophysique Interne et Tectonophysique (LGIT), UMR CNRS 5557, University Grenoble I, France

³Géosciences Rennes, UMR CNRS 6118, University Rennes, France

⁴International Institute of Earthquake Engineering and Seismology (IIEES) Tehran, Iran

⁵OrsayTerre, UMR CNRS 8616, University Paris XI, France

Accepted 2004 December 10. Received 2004 November 4; in original form 2004 July 22

SUMMARY

The Zendan–Minab zone is the transition zone between the Zagros collision to the west and Makran subduction to the east. It is also linked to the north with the Nayband–Gowk fault system that bounds the Lut Block to the east. The total convergence rate between Arabia and Eurasia is estimated to range between 23 and 35 mm yr⁻¹ in a NNE-trending direction. The deformation through the Minab–Zendan system is accommodated within two fault systems, the western N160°E-trending Minab–Zendan fault system and the eastern north–south Sabzevaran–Jiroft fault system. The study area is characterized by a well-defined succession of Quaternary deposit levels. The age of these deposits was estimated by archaeological data, regional palaeoclimate correlations and constrained by additional *in situ* ¹⁰Be dating in another paper in this study. These deposits exhibit offsets, both lateral and vertical, that are evaluated by satellite image analysis and GPS profiles. Thanks to offsets and ages the strike-slip rates associated with the Minab–Zendan and the Sabzevaran–Jiroft fault systems are calculated to be 5.1 ± 1.3 or 6.6 ± 1.5, and 6.2 ± 0.7 mm yr⁻¹, respectively. These results allow an evaluation of the velocity vector of the Musandam Peninsula (Oman) with respect to the Lut Block of 11.4 ± 2.0 or 12.9 ± 2.2 mm yr⁻¹ in a N10 ± 15°E direction, close to the GPS estimates. This study also constrains the in-plane slip rates for each fault.

Previous works indicate that the Zagros accommodates only 10 mm yr⁻¹ of shortening, while 10 mm yr⁻¹ should be accommodated by the Alborz mountains in northern Iran. This last 10 mm yr⁻¹ may be accommodated through the Nayband–Gowk system and the East Iranian ranges, implying that the two fault systems constituting the Zagros–Makran transfer zone have different geodynamic roles. The western Minab–Zendan fault system links the Makran and Zagros deforming zones, whereas the northwestern Jiroft–Sabzevaran fault system is transmitting the deformation to the Nayband–Gowk system and then to the Alborz ranges. The presence of another such strike-slip zone within the Makran seems to indicate that the accommodation zone between the Zagros and Makran is wide, of the order of 400 km. We interpret this deformation pattern that accompanies the genesis of the immature transform zone by a flexure of the slab under the Zagros–Makran transfer zone instead of a tear in the slab that may be expected to induce a sharper transition zone.

Key words: differential GPS, fault, Iran, Makran, geomorphology, Zagros.

1 INTRODUCTION

Iran is located within the convergence domain between the Arabian and Eurasian plates. The Arabian–Eurasian convergence off the Hormoz Strait (26.5°N; 56.5°E) is trending north to NNE

*Now at: Laboratoire des Mécanismes de Transfert en Géologie (LMTG), UMR CNRS-IRD 5563, University P. Sabatier Toulouse III, France. E-mail: regard@lmtg.obs-mip.fr.

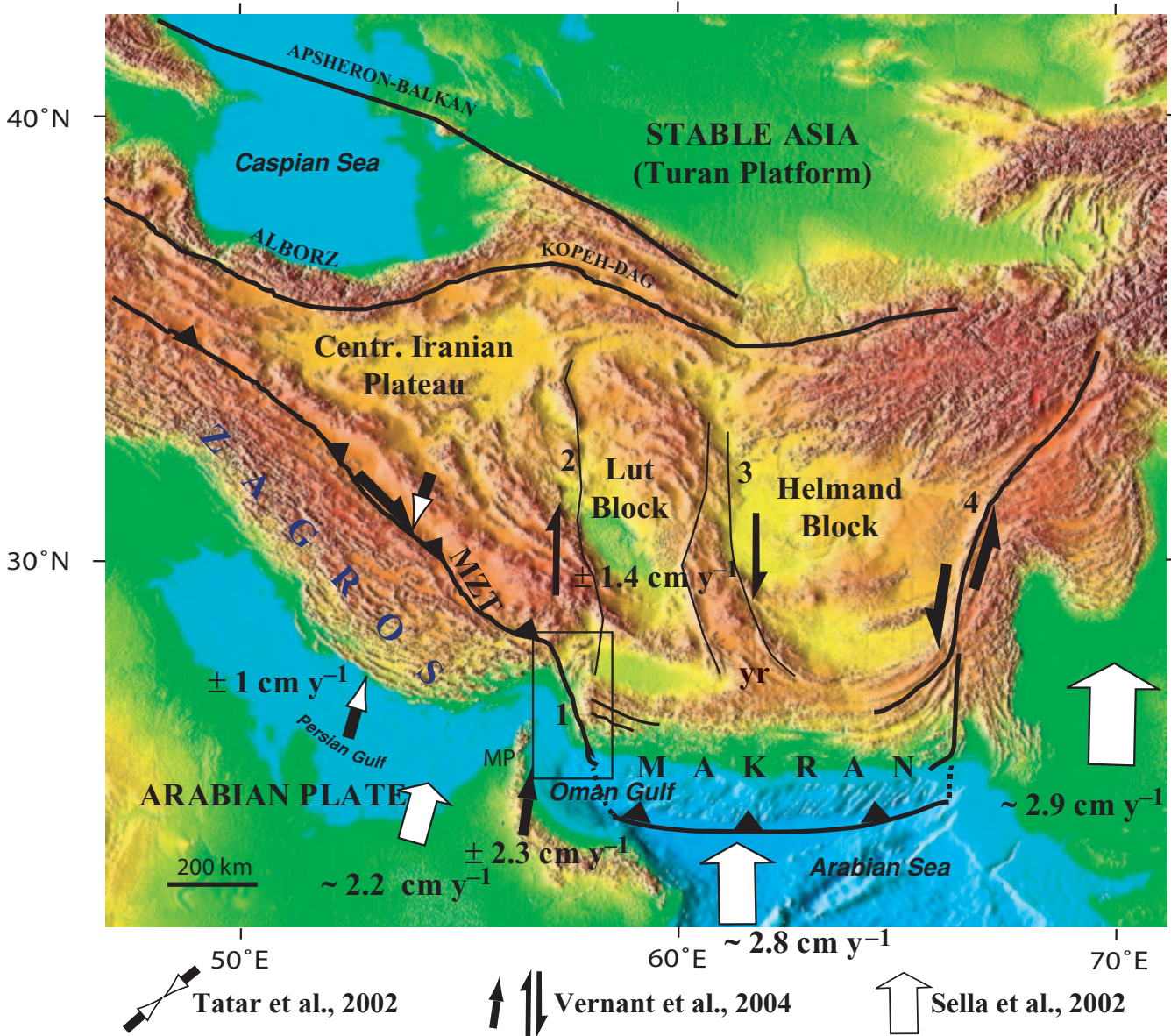


Figure 1. Geodynamic setting of Iran and adjacent areas. The main geodynamic structures are indicated and the study area is indicated by an open rectangle. In this paper we mention the evaluations of GPS relative motion between Arabia and Eurasia of Sella *et al.* (2002) and Vernant *et al.* (2004). The estimate of the Zagros shortening comes from the GPS study of Tatar *et al.* (2002), and that of strike-slip motion on the boundaries of the Lut Block is from Vernant *et al.* (2004). 1, Minab–Zendan fault system; 2, Nayband–Gowk fault system; 3, Neh–Zahedan fault system (East Iranian ranges); 4, Chaman fault; MZT, Main Zagros Thrust.

(Fig. 1). Estimates of the convergence rate range from 35 mm yr^{-1} according to the NUVEL-1 model (DeMets *et al.* 1990) to about $23\text{--}25 \text{ mm yr}^{-1}$ deduced from GPS measurements (Bayer *et al.* 2003, 2005; McClusky *et al.* 2003; Vernant *et al.* 2004). The northwest-striking Zagros fold and thrust belt is an active continental collision zone that corresponds to a continental accretionary prism within the Arabian Plate, which accommodates about 10 mm yr^{-1} of NNE-trending shortening, between Arabia and Asia (Alavi 1994; Talebian & Jackson 2002; Tatar *et al.* 2002; Blanc *et al.* 2003). To the east, the east-striking Makran belt is the emerged portion of an accretionary prism resulting from the subduction of the Oman Gulf oceanic lithosphere beneath the Iranian Platelet (Byrne *et al.* 1992; McCall 1997; Kopp *et al.* 2000). A NNW-trending deformation zone, the oblique reverse-dextral Minab–

Zendan fault system, connects the western Makran to the eastern Zagros deformation domains (Fig. 2) (McCall & Kidd 1982; Regard *et al.* 2004).

Zagros is a northwest-trending fold and thrust belt made up of a 6 to 15 km thick sedimentary pile which overlies a Precambrian metamorphic basement (McCall *et al.* 1985; McCall 1997). The sedimentary cover can be divided into three successive sequences: Precambrian to lowermost Cambrian shallow water platform deposits with thick evaporitic layers at the base; a Carboniferous to Cretaceous carbonate sequence platform (Faure-Muret & Choubert 1971; Farhoudi 1978); and uppermost Cretaceous to Recent synorogenic deposits which consist of intertongued platform carbonates and siliclastic sediments (Alavi 1994). GPS measurements estimated that $10 \pm 4 \text{ mm yr}^{-1}$ of shortening is currently absorbed by the

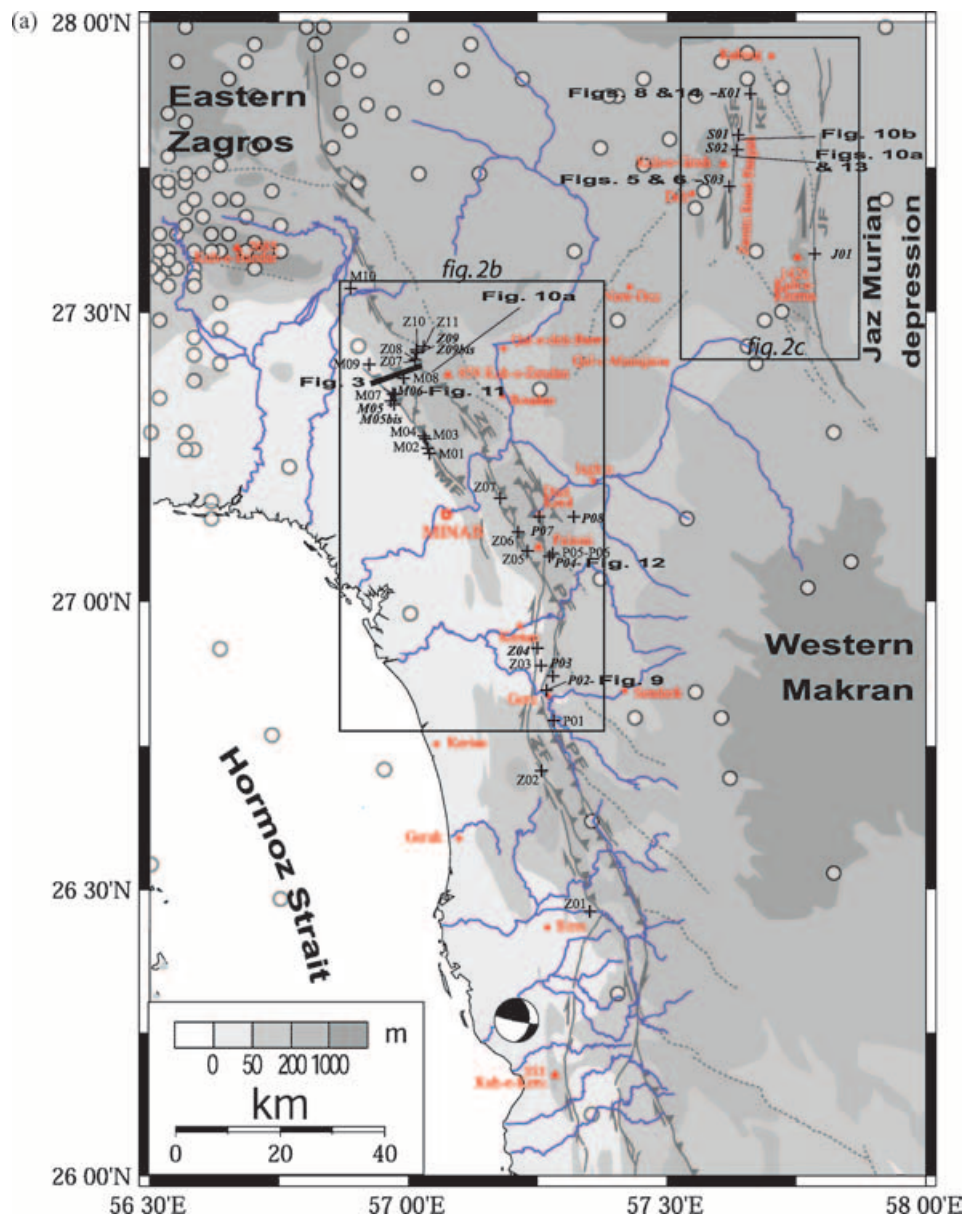


Figure 2. (a) Map of the study area and the active faults therein. Continuous lines are the confirmed active faults and dashed lines the active faults inferred from satellite images (Regard *et al.* 2004). We add the sites visited during the field study. Sites labelled in bold italic type are sites where fault slip offsets were measured. Triangles show the main mountain summits and circles are villages. Open circles represent the seismicity recorded by global seismological networks for the period 1973–2002 (NEIC 2002). JF, Jiroft Fault; KF, Kahnuj Fault; MF, Minab Fault; PF, Palami Fault; SF, Sabzevaran Fault; ZF, Zendan Fault. The locations of the cross-section of Fig. 3 and of the other figures are shown. The only focal mechanism clearly related to the zone corresponds to a CMT solution (CMT 2002). Parts (b) and (c) are enlargements of parts of (a) for the Minab area and for the Jiroft–Sabzevaran fault system area, respectively.

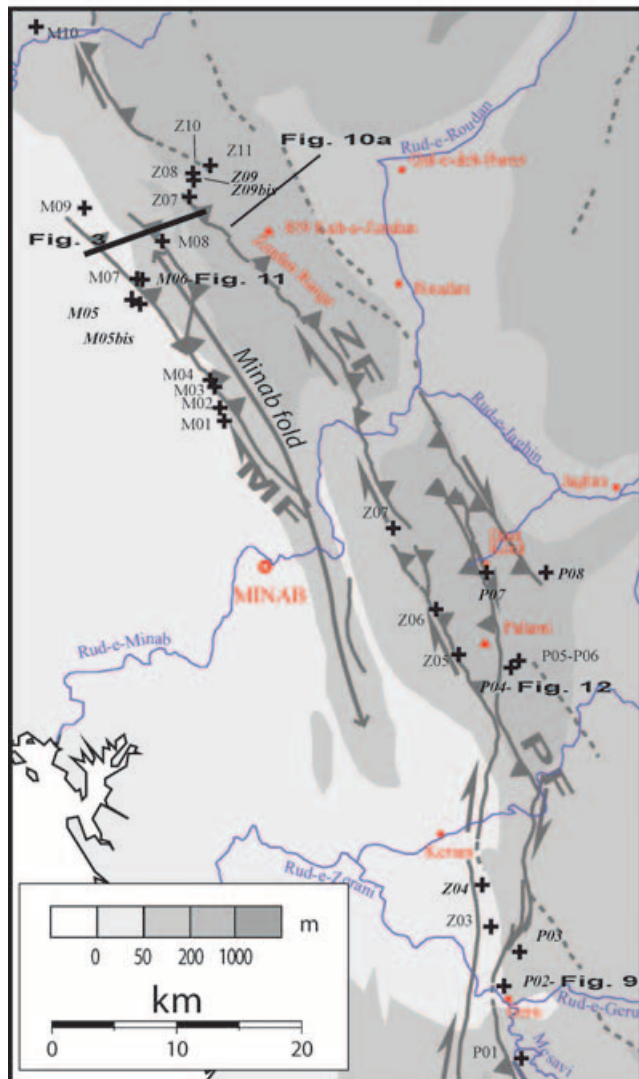
Central Zagros deformational belt (Tatar *et al.* 2002). This value is in agreement with the long-term deformation rate determined from balanced cross-sections by Blanc *et al.* (2003).

Active since the Late Oligocene (Harms *et al.* 1984), the Makran is an accretionary wedge fed by detrital sediments from the Himalayan belt and deposited in the Arabian Sea and the Gulf of Oman (Garzanti *et al.* 1996; Fruehn *et al.* 1997; Kopp *et al.* 2000). Its mean elevation is about 1500 m and its across-strike width 400–600 km (Byrne *et al.* 1992). The wedge front propagates seawards with an estimated rate of about 10 mm yr^{-1} (White 1982).

North of the active accretionary belts, the Eurasian Plate is deformed in its interior up to 40° north on the east-striking Alborz

and Kopet-Dagh mountain belts (Fig. 1). Between the two belts, the deformation is accommodated by two large-scale fault belts, namely the Nayband–Gowk and Neh–Zahedan north-trending fault systems, separating the relatively undeformed Central Iran, Lut and Helmand blocks (Fig. 1). The lateral displacement along the Nayband–Gowk and Neh–Zahedan fault systems has been estimated as about 2 mm yr^{-1} (Walker & Jackson 2002) and 15 mm yr^{-1} , respectively (Freund 1970; Tirrul *et al.* 1983; Walker & Jackson 2002). The rates estimated in Walker & Jackson (2002) made the assumption that the faults are 5 Myr old, and that the present-day shear across eastern Iran is $20\text{--}25 \text{ mm yr}^{-1}$ based on global plate circuits. It is now known from GPS that there is only 15 mm yr^{-1} of shear in

(b)



(c)

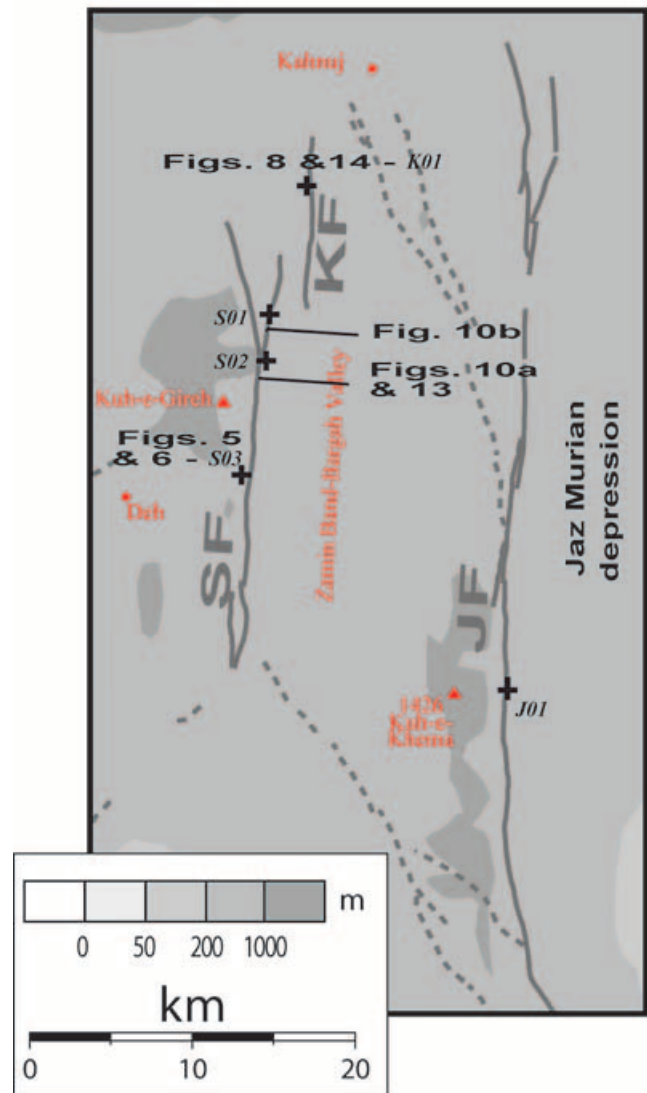


Figure 2. (Continued.)

eastern Iran (Vernant *et al.* 2004), and so the rates implied for the Sistan faults in Walker & Jackson (2002) are probably too high. The main point here is that the total amount of shear in the eastern Iranian ranges is much more than across the Gowk–Nayband Fault. The Central Iranian Plateau is moving northwards with respect to Eurasia with a velocity deduced from GPS measurements of 13 ± 2 mm yr⁻¹ (Nilforoushan *et al.* 2003; Vernant *et al.* 2004), or of 15–20 mm yr⁻¹ from reconstruction based on NUVEL-1 (DeMets *et al.* 1990; Jackson *et al.* 1995, 2002), this convergence velocity being accommodated through the Alborz and the Apsheron–Balkan belts. To the east, the Lut Block drifts northwards at a rate of about 6.5 ± 2 mm yr⁻¹, while the Helmand Block does not seem to move with respect to Eurasia (Walker & Jackson 2002; Vernant *et al.* 2004).

Seismicity, as recorded by global seismic networks and historical records (Berberian & King 1981; Kadinsky-Cade & Barazangi 1982; NEIC 2002), indicates a relatively low level of seismic activity in the study area, shallow earthquakes being mainly located within the Zagros as a wide seismic cluster, northwest of the Minab–Zendan fault system (Fig. 2).

The NNW-trending reverse-dextral Minab–Zendan fault system permits transfer of the deformation from the Zagros to the Makran

prisms. Taking into account its location at the plate boundary and its NNW trend that is drastically oblique with respect to the direction of the convergence, the Minab–Zendan fault system could have two major roles on a lithospheric scale: (1) to accommodate the plate convergence obliquity and (2) to transform the Zagros collision process into the Makran subduction. Preliminary study shows that this transfer is accommodated by combined reverse and right-lateral faulting, distributed over a wide domain (Regard *et al.* 2004). To the west, three major NNW-trending faults constitute the Minab–Zendan fault system, the Minab, Zendan and Palami faults, while three north-trending faults, the Sabzevaran, Jiroft and Kahnuj faults (Jiroft–Sabzevaran fault system, Fig. 2), affect the eastern part of the studied zone.

Tectonic study and fault slip-vector analyses indicate that two distinct tectonic regimes have occurred successively since the Miocene within a consistent regional northeast-trending compression (Regard *et al.* 2004):

(1) A Late Miocene to Pliocene tectonic regime characterized by partitioned deformation, between reverse faulting and right-laterally arranged *en echelon* folding.

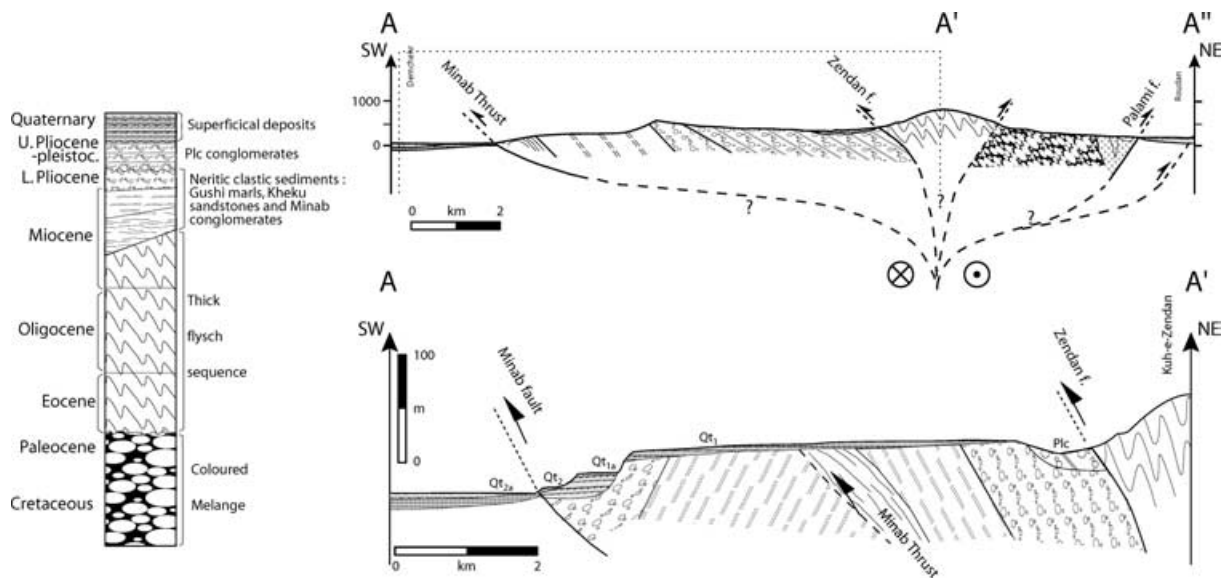


Figure 3. Schematic profile through the Minab anticline and the Zendan chain (see Fig. 2 for location). The faults within the cross-section suggest a flower structure. A–A'–A'': entire cross-section. A–A': zoom of section A–A'' (highlighted by the dashed line over section A–A'')—unscaled schematic cross-section showing the stratigraphic position of the Quaternary alluvial deposits. Left: stratigraphic sequence of the Minab area, including Quaternary terraces, modified after McCall (1997).

(2) Since Middle–Late Pliocene, a N45°E-trending σ_1 axis transpressional regime that homogeneously affects the region, mainly producing faulting.

This last regime corresponds to the present-day one and produces reverse-dextral displacements along the Minab–Zendan fault system. Only one large earthquake ($M_w = 5.9$, 1983 July 2, latitude 26.3°N, longitude 57.2°E; Fig. 2) recorded by the global seismic network highlights the activity of the present-day kinematics of the studied area. The focal mechanism provided by the Harvard CMT database gives evidence for a right-lateral component on a N05°E-trending (for a dip of 42°E) focal plane (Dziewonski *et al.* 1981; CMT 2002), consistent with the regional orientation of the structures and agreeing with the fault system kinematics. The Minab, Zendan and Palami faults connect the Main Zagros Thrust (MZT) with different thrusts of the inner Makran. Consequently, the total expected slip rate of the Minab–Zendan fault system is increasing northwards, by the progressive addition of the slip of each Makran thrust. In addition, the Jiroft–Sabzevaran fault system is linked to the north with the Nayband–Gowk fault system, contributing to transfer convergence deformation northward of Iran, i.e. to the Alborz and Kopet-Dagh deformation belts.

Here we present a quantitative analysis of the Quaternary slip rate of each individual fault segment of the fault systems based on detailed mapping of the active fault traces using SPOT images, aerial photographs and field survey. The investigated area extends over the transition zone between Zagros and Makran, northeast of the Hormoz Strait. On selected sites, a detailed survey of surface morphology has been made using topographic linear profiles with differential GPS. The age of deformation has been estimated by dating Quaternary alluvial fan abandonments using *in situ*-produced ^{10}Be concentrations and/or deduced from archaeological investigations (Regard 2003). This data set will furnish solid constraints to define the role of the both Minab–Zendan and Jiroft–Sabzevaran fault systems within the accommodation of the relative motion between the Arabian, Iran and Lut blocks and Eurasia.

2 QUATERNARY GEOMORPHIC FEATURES

2.1 Sequence defined in the western part of the studied zone

Pre-Quaternary formations cropping out in the studied zone have been intensively folded and uplifted during the Late Tertiary tectonic event. Since the Pleistocene, erosion of the resulting relief has produced piedmont spreading deposits at the foot of the range escarpments. These series of Quaternary alluvial and colluvial sandy conglomerate deposits constitute the youngest formations. Their succession corresponds to a Quaternary morphoclimatic sequence previously described by Dufaure *et al.* (1978) (see also Dufaure 1984; McCall *et al.* 1985, and Fig. 3).

During a Middle Pleistocene wet episode, folds and thrusts were dissected by the drainage network and unconformably overlain by detritic materials (mainly sandy conglomerates) forming a primitive pediment produced by a sheetflood episode (Fig. 3). During this period, the western slope of the Zendan range was levelled to produce a west-dipping pediment planation of regional extent (labelled Qt_1 in the Minab quadrangle of McCall *et al.* 1985). The resulting primitive pediment morphology is a regional geomorphic surface marked by the absence of bars and swales and by the occurrence of well-developed desert pavement, and that dips slightly westwards. Geological, geomorphological and archaeological arguments (Upper to Late Acheulian industry sampled at the surface top by Thibault, unpublished work, 1977; Dufaure *et al.* 1978) suggest an approximately Middle Pleistocene age for the sedimentary episode that produced the primitive pediment (Acheulian is thought to end at around 100 ka, but its boundaries are spatially varying and not well defined in Iran). This surface may have formed during a humid period corresponding to the deglaciation between isotopic stages 6 and 5e, before the setting of the last interglacial conditions (~125 ka).

A second generation of pediment (Qt_{1a} , Fig. 3) dated from the early Late Pleistocene (Dufaure *et al.* 1978) corresponds mainly to

coarse anastomosed alluvial terraces. This second pediment surface provides less developed desert pavement (a less 'regified' surface) and displays Mousterian (Middle Palaeolithic) industry, consistent with an early Late Pleistocene age (~40 ka). Again, Mousterian is not well defined in Iran; in Europe it is thought to last from ~100 to ~35 ka).

The last depositional phases correspond to two Late Pleistocene and Holocene generations of alluvial fan deposits. In the study area, those fans are entrenched by cut and fill processes as a consequence of lowering of the base level as a result of major external influences such as tectonism and climatic changes (e.g. Schumm *et al.* 1987). The spatial relationships between the alluvial fans lead to subdivision of the alluvial fans into two units. The youngest fans, (Qt_{2a} in the Minab quadrangle, McCall *et al.* 1985), cone shaped in plan view, are slightly incised. During deposition, they truncated parts of the older fans, Qt₂, which are affected by stream carving. Stratigraphically lower than Qt_{2a}, the Qt₂ fans present slightly degraded shapes inherited from the emplacement of the Qt_{2a} alluvial fans (Fig. 3). They are made of poorly consolidated fanglomerate comprising coarse debris (mainly cobbles and abraded boulders) interbedded with silt and sand levels. Although outcrop conditions are fairly good, no significant difference in weathering has been observed between Qt₂ and Qt_{2a} fan surfaces. Nevertheless the two generations of fans can be easily distinguished on aerial photographs by their differential elevations, as well as by the different degree of incision of their surfaces. Epi-Palaeolithic (or Mesolithic) industry has been found on the Qt₂ fan surfaces, suggesting an uppermost Late Pleistocene age for the abandonment of the Qt₂ surfaces that could correspond to the initiation of the deglaciation ending the Last Glacial Maximum (end of stage 2) (Sanlaville 1992). Therefore its emplacement was achieved during the last major humid period related to glacial termination while younger Qt_{2a} emplaced during a minor humid period during the Holocene. These two generations (Qt₂ and Qt_{2a}) of well-preserved fans can be correlated with alluvial terraces recognized within the Zendan range and with alluvial fans observed within the Rudan and Jaz Murian depressions, particularly on the eastern slopes of the Zendan range and the Sabzevaran and Jiroft horsts (see Fig. 2 for location).

Younger deposits, consisting of sand deposits, crop out within the coastal plain between the folded domain and the sea.

2.2 Correlation with the alluvial fan sequences cropping out in the eastern area

In the eastern part of the study area, that is to say to the east of the Zendan and Palami faults (Fig. 2), McCall *et al.* (1985) applied the same labels as in the western, coastal, part for Late Quaternary deposits, even if their geomorphic characteristics are not strictly similar on both sides of the Zendan range. Combined geomorphic studies (SPOT image and field analyses) indicate that the eastern domain of the Zendan range, i.e. the Rudan Depression and the Jiroft–Sabzevaran fault system frontal alluvial plains, comprises four alluvial fan units. Successive generations of fans can be distinguished by relative elevation, degree of surface erosion and incision and relative levels of regification, marked by the intensity of dark desert varnishing at their surface. Even in satellite images, they appear with strong colour variations, white, light grey or dark (Fig. 4):

(1) The lowest white fans are the youngest and represent the current active fans. Coarse materials (up to metre-scale) lie at their surface. By correlation with the Minab area to the west, they are labelled Qt_{2a}.

(2) Light grey fans are partly regified. They are labelled Qt₂ but sometimes include deposits that are related to the Qt_{2a} deposits of the Minab area. To avoid confusion, we labelled them as Qt_{2*}.

(3) Dark grey fans correspond to highly regified fans, whose surface is dark on satellite images as well as in the field. They do not correspond to a single event since at least two generations of 'dark fans' are observed. They are both labelled Qt_{1a} on the map by McCall *et al.* (1985). Thus, new labels have been added to avoid confusion: Qt_{1a} for the youngest of them (~20 ¹⁰Be kyr, see the following), and Qt_{1a*} for the oldest (~45 ¹⁰Be kyr).

2.3 Age of Quaternary surfaces

Accurate chronological records are critical for understanding landform evolution, and, in particular, alluvial fan emplacement sequences during local/global climatic changes. We measured *in situ*-produced ¹⁰Be in quartz boulders exposed on the top surfaces of Late Quaternary sequences; ¹⁰Be ages given hereafter correspond to weighted means (*cf.* Table 1). ¹⁰Be dating is used similarly by Brown *et al.* (1991), Siame *et al.* (1997) and Braucher *et al.* (2000). Details of the dating of these exposures are reported in a companion paper (*cf.* Regard 2003; Regard *et al.* 2005), where ¹⁰Be ages are compared with archaeological data and chronologies (collected and processed by C. Thibault in 1977) to constrain the ages of the successive depositional periods and to provide an insight into the regional palaeoclimatic correlation. In the following we summarize the major conclusions, highlighting the chronology of the abandonment of the successive Quaternary deposit sequences and climatic events:

(1) The lowest (younger) fan/terrace level was deposited during the Holocene optimum (see, among others, Bar-Matthews *et al.* 1997; Burns *et al.* 1998; Fontugne *et al.* 1999; Burns *et al.* 2001; Glennie & Singhvi 2002; Hoelzmann *et al.* 2003; Bar-Matthews & Ayalon 2005), between 5 and 9 kyr BP. ¹⁰Be ages indicate a surface abandonment at 5.7 ± 0.6 ¹⁰Be kyr. This age is calculated for surfaces of fans deposited at the fronts of both the Minab and Sabzevaran faults, while at the front of the Palami Fault escarpment, fan surfaces are dated at 9.2 ± 1.0 ¹⁰Be kyr. However, this seems to correlate with the same climatic/deposition event.

(2) The abandonment of the second Quaternary deposit sequence is well defined thanks to epi-Palaeolithic industries sampled at its regional surface. They indicate for this stage an age older than 10 kyr. It is consistent with the calculated exposure age of 13.6 ± 1.1 ¹⁰Be kyr, which in addition is in agreement with a regional climatic period reported at about 12 kyr BP (Sanlaville 1992; Yan & Petit-Maire 1994; Bar-Matthews *et al.* 1997).

(3) A wet period between 22 and 30 kyr BP is well defined throughout the region (Clark & Fontes 1990; Sanlaville 1992; Fontugne *et al.* 1999). The local 20.3 ± 1.9 ¹⁰Be kyr age for Sabzevaran cannot be strictly related to it in a first approximation. This can, however, be explained in two ways: either, since the minimum ¹⁰Be exposure ages are calculated assuming negligible erosion, a low but significant erosion rate will imply an increase of that ¹⁰Be age over 22 kyr or the fan deposition results from local effects such as uplift. Thus, in the following, the ¹⁰Be exposure age of 22.1 ± 1.6 ¹⁰Be kyr determined on correlated features will be used (*cf.* Table 1).

(4) Both ¹⁰Be exposure ages (mean 49.0 ± 3.8 ¹⁰Be kyr) and regional records document an important humid and depositional period between 40 and 50 kyr BP (Sanlaville 1992; Yan & Petit-Maire 1994; Hoelzmann *et al.* 2003). Because of the dispersion of the ¹⁰Be ages the value of 42 kyr BP from the literature is preferred; an arbitrary error of 10 per cent is associated with it. It may not be

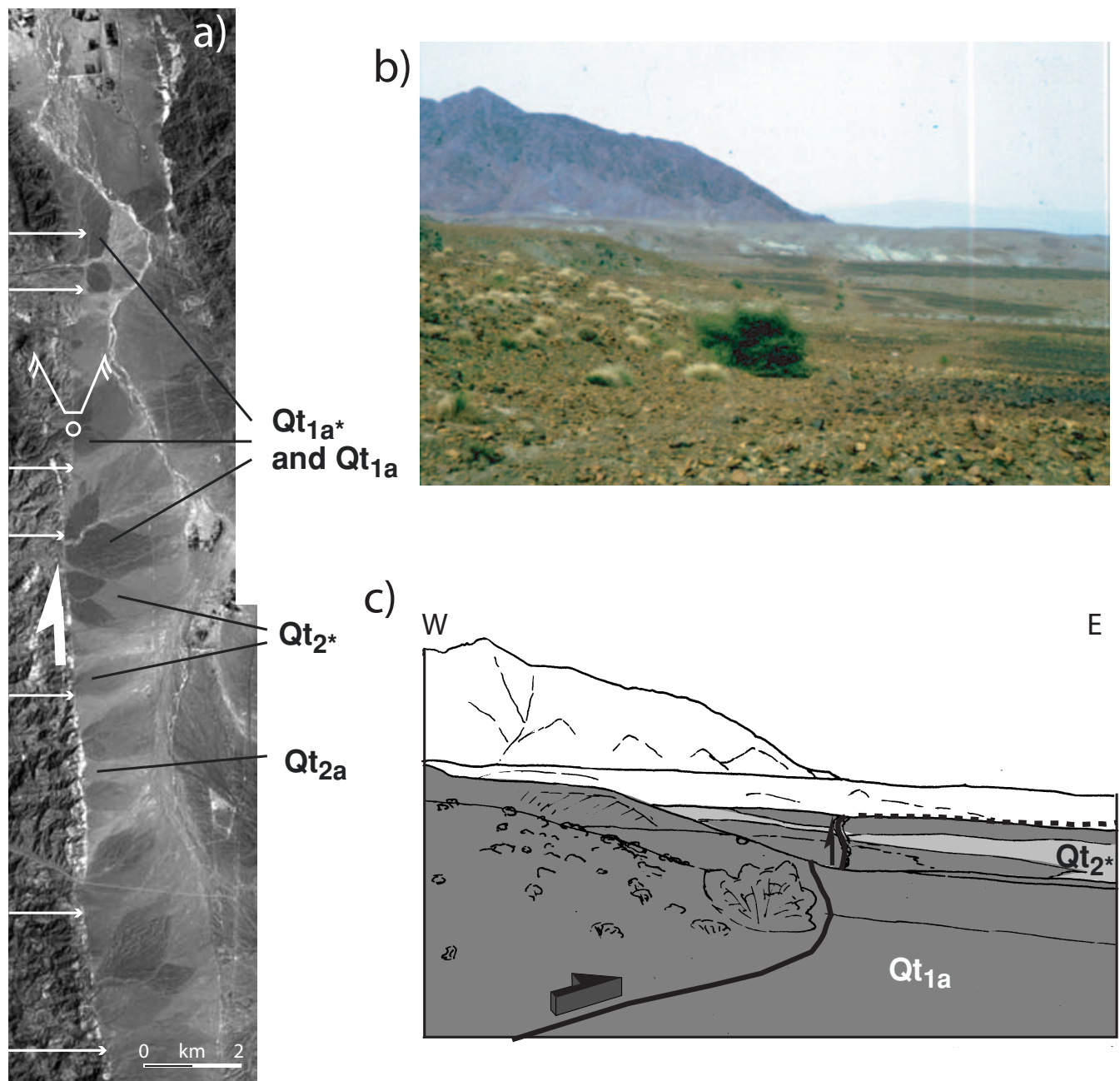


Figure 4. (a) SPOT satellite image of the Sabzevaran Fault. White arrows highlight its trace. The open circle gives the location of site S02 with the direction of photograph (b). The fan sequence is clearly highlighted by the different coloration of the fans; this is due to the degree of regification of each fan surface (evolution toward a desert pavement). (b), (c) North-facing view of the Sabzevaran Fault at site S02 and interpretative sketch. The different fan colorations are clearly visible (modified after Regard *et al.* 2004).

associated with Mousterian industries since they are thought to end near 50 kyr BP.

(5) Older humid periods are reported at around 65–70, 80, 115–120 (highly reliable), 180–210 and 300–325 kyr BP, the last two being suggested by only one team (Burns *et al.* 1998; Burns *et al.* 2001). Deposits associated with the Acheulian industry were most likely emplaced during the 115–120 kyr BP or 180–210 kyr BP humid periods. For calculations we infer an error of 10 per cent.

In summary, Dufaure *et al.* (1978) (see also Dufaure 1984) first established that the Minab area, located in the western part of the

studied zone, is characterized by Quaternary alluvial deposits stratigraphically organized in a four-level sequence. Previous investigation (Regard *et al.* 2004) indicates that Quaternary alluvial deposits can be found all over the studied zone (see also McCall *et al.* 1985) and that much of them are cross-cut by the fault traces and display evidence of offsets caused by fault motion. We previously estimated the ages of these deposits with the archaeological industries discovered by Thibault (e.g. Thibault, unpublished work, 1977), and with ^{10}Be dating (Regard 2003; Regard *et al.* 2005). The first deposit of the Dufaure *et al.* (1978) classification (Qt_{2a}) is an alluvial terrace dated between 5 and 9 kyr BP. According to our study, the second level (Qt_2) corresponds to terraces or fan surfaces

Table 1. ^{10}Be calculated surface abandonment ages (e.g. Regard 2003; Regard *et al.* 2005). The assumption of negligible erosional loss results in a calculated lower limit for surface exposure ages (Brown *et al.* 1991; Cerling & Craig 1994). The minimum exposure ages presented here have been calculated using ^{10}Be production rates estimated from the altitude- and latitude-dependent polynomials of Lal (1991). The associated uncertainties result from analytical uncertainties based on counting statistics (1σ) conservative assumptions of 3 per cent variability in machine response, a 50 per cent uncertainty in the chemical blank correction and, mainly, from 10 per cent error associated with calculated production rates. ^{10}Be indicate the abundance of ^{10}Be in sample, and the *a priori* level indicates the deposit age expected, after the field work and the mapping from McCall *et al.* (1985). Average weighted values and corresponding uncertainties are calculated for the different deposition stages.

Site	<i>A priori</i> level	Sample	^{10}Be (10^4 atoms g^{-1})	^{10}Be error (10^4 atoms g^{-1})	Production (atoms g^{-1} yr^{-1})	Age (yr)	Age error (yr)
M05bis	Qt ₂	VR00-1	6.28	0.906	5.0	12 592	1815
M05bis	Qt ₂	VR00-2	6.53	0.968	5.0	13 095	1939
M05bis	Qt ₂	VR00-3	9.11	1.42	5.0	18 271	2846
M06	Qt ₂	VR00-5	2.60	0.472	5.0	5182	940
M06	?	VR00-9	11.4	1.60	5.0	22 990	3206
M09	Qt ₁	VR00-11	15.7	3.18	5.1	30 977	6278
M09	Qt ₁	VR00-12	15.7	3.60	5.1	31 022	7108
M09	Qt ₁	VR00-13	89.8	22.4	5.1	183 984	45 996
M09	Qt ₁	VR00-15	11.3	1.79	5.1	22 359	3535
Z04	Qt ₂ or Qt _{2a}	VR01-16	5.85	1.49	4.7	12 383	3160
P07	Qt ₂	VR00-23	5.51	1.01	6.2	8881	1632
P07	Qt ₂	VR00-24	4.95	0.899	6.2	8006	1452
P07	Qt ₂	VR00-25	7.80	1.35	6.2	12 573	2179
S01	Qt _{1a}	VR01-5	47.7	5.89	6.8	71 216	8787
S01	Qt _{1a}	VR01-6	27.2	3.73	6.8	40 225	5520
S01	Qt _{1a}	VR01-8	33.0	4.38	6.8	49 069	6515
S02	Qt _{1a}	VR01-02	12.4	2.05	7.0	17 765	2942
S02	Qt _{1a}	VR01-3	12.2	2.05	7.2	17 199	2884
S02	Qt _{1a}	VR01-4	26.8	3.66	7.1	38 018	5190
S03	Qt _{2a}	VR00-20	4.73	0.887	7.9	5991	1125
S03	Qt _{2a}	VR00-21	7.78	2.19	7.9	9873	2778
S03	Qt _{2a}	VR00-22	4.30	0.890	7.9	5449	1127
S03	Qt _{2a}	VR01-19	4.37	0.915	7.5	5842	1222

assigned to the epi-Palaeolithic, from the industries they display and dated at 13.6 ± 1.1 ^{10}Be kyr. In the Minab area, the third level of the Dufaure *et al.* (1978) classification (Qt_{1a}) displays Mousterian industries (100–50 kyr BP). ^{10}Be exposure ages performed on geomorphologically related fans near the Sabzevaran Fault yield two distinct deposition events at 22.1 ± 1.6 ^{10}Be kyr and 42 ± 4.2 kyr (respectively Qt_{1a} and Qt_{1a*}). Finally, according to the industries it displays, the highest level of the Dufaure *et al.* (1978) classification (Qt₁) is assigned to the Late Acheulian age (300–100 kyr BP). However, there may be depositional gaps in the Minab area where Dufaure (1984) established their classification, and this highest level may correspond to one of the deposition stages described in the literature for that time interval, that is at around 65–70, 80, 115–120, 180–210 or 300–325 kyr BP.

3 METHODOLOGY FOR OFFSET CALCULATIONS

Through the study domain, the faults offset the geomorphic features right-laterally as streams, Late Quaternary alluvial fans, etc. The faceted spurs and vertical scarps that also mark the fault traces indicate a coeval lateral and reverse faulting, i.e. an oblique dextral-reverse fault slip.

Horizontal/vertical cumulative offsets of the studied geomorphic features were attempted by surveying surface morphology. Differential GPS using two Trimble PRO XRS receivers (one as a base, generally upstream from the fault scarps, the other one mobile, attached to a hand carried pole) was used to measure three different kinds of topographic profiles:

- (1) profiles perpendicular to the fault scarp;
- (2) profiles parallel to the fault trace on both sides of the fault scarp (i.e. upstream and downstream domains) to reconstruct the surface shape of the Quaternary deposits, for example the surface shape of the fan envelope;
- (3) profiles all along-strike river streams, i.e. from upstream to downstream through the fault trace.

After the survey, positioning data were processed by Asset Surveyor and Pathfinder Office Trimble software. When data points were dense enough, a local digital elevation model (DEM) was processed (Fig. 5).

Vertical offsets were estimated from profiles perpendicular to the fault scarp. Theoretically, the envelopes of the footwall and hangingwall topographic slopes are parallel. As currently used in active tectonic studies, the vertical offset is therefore deduced from the vertical distance between both envelope slopes (Fig. 6) (Avouac 1993; Gaudemer *et al.* 1995; Carretier *et al.* 2002). However, the two envelopes are often not strictly parallel; in this case measurements were made as close as possible to the scarp location to obtain the best possible measurement. Moreover, sometimes the fans present a rough shape due to morphogenetic processes (such as erosion) affecting the abandonment surfaces. The profiles that indicate badly preserved surfaces are rejected.

In many cases the alluvial surfaces we dealt with were mountainous alluvial fans with a characteristic conical shape. When offset by a fault, their upper and lower slopes are not in continuity (Fig. 7). The 3-D shape of the fan then permits us to reconstruct the relative position of the upthrown and downthrown walls before fault motion. In turn, we used this property to obtain a graphic estimate through

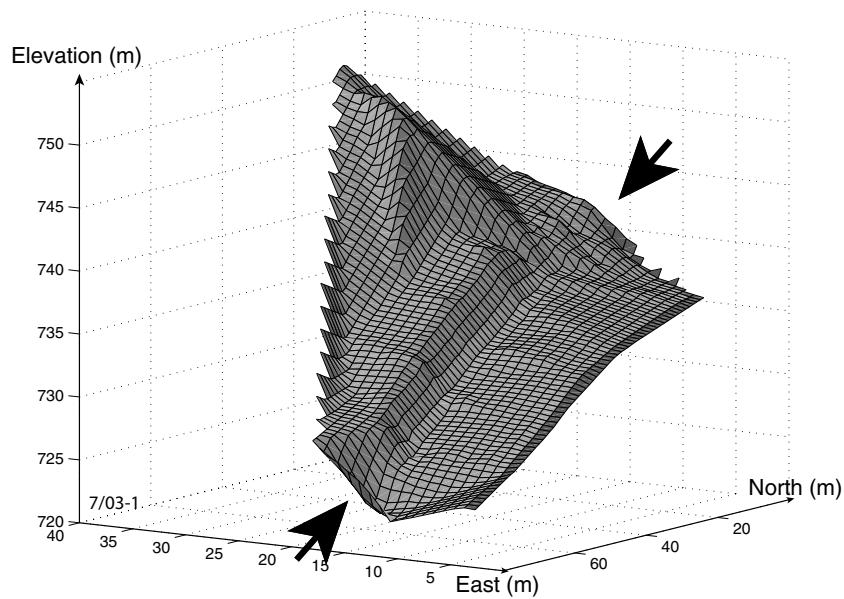


Figure 5. 3-D drawing of a digital elevation model of location S03 on the Sabzevaran Fault. It is measured by differential GPS and interpolated from 2-D profiles by Matlab software. The fault trace is indicated by black arrows.

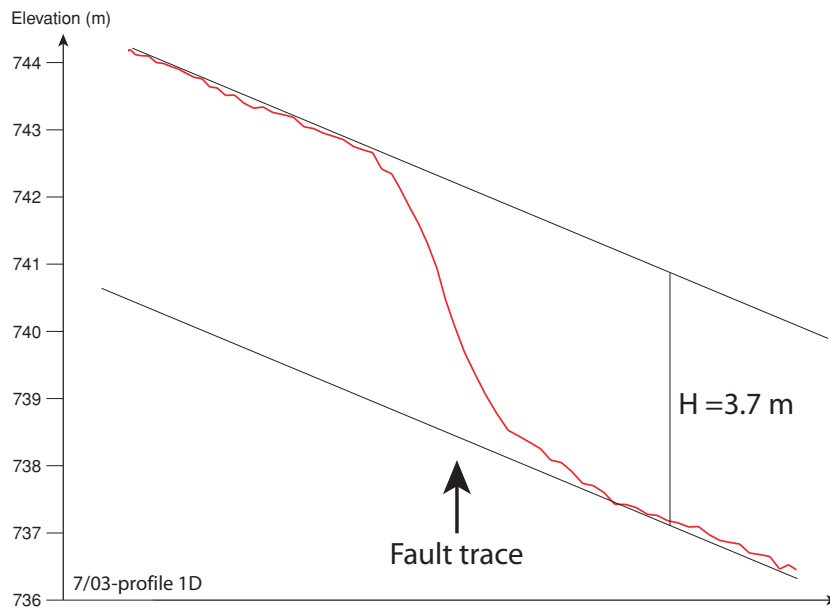


Figure 6. Profile D measured at location S03 on the Sabzevaran Fault. The same mean slope is found for the hangingwall and footwall slope envelopes. The vertical distance between the two slope envelopes is measured to 3.7 m. It is assumed to be the vertical offset due to the fault whose superficial trace is indicated by the black arrow.

superposition of the upper and lower parallels to the fault profiles (*cf.* Fig. 8).

Usually, vertical offsets are better defined than the horizontal ones. Horizontal offset can be indirectly calculated knowing the vertical displacement, slip-vector (given by striae measurement) and fault plane geometry (azimuth and dip), as illustrated in Appendix A.

Upstream to downstream profiles through the fault trace along river streams provide direct measurement of the lateral stream offset. Indeed, in geographical coordinates these stream profiles allow a direct measurement of the cumulative horizontal offset due to a fault since the most recent of two important events—the beginning of fault activity or the set-up of the hydrographic network. This

procedure consists of removing the effects of the fault motion by calculating the backward motion of the fault that removes the kinks of streams. Care must be drawn on the possibility of stream captures (Gaudemer *et al.* 1989). In this study, graphical methods were used to determine such horizontal offsets (see, for example, Fig. 9).

To complement these detailed surveys, SPOT images and aerial photographs have been used to map the active fault traces and the horizontal along-strike offsets, through examination of fan edges, fan envelopes and streams incising Quaternary deposits exhibiting large right-lateral offsets. A new method consisting of localizing the fan median, both in the hangingwall and the footwall, was also tried. The median is assumed to be the straight line at an equal distance

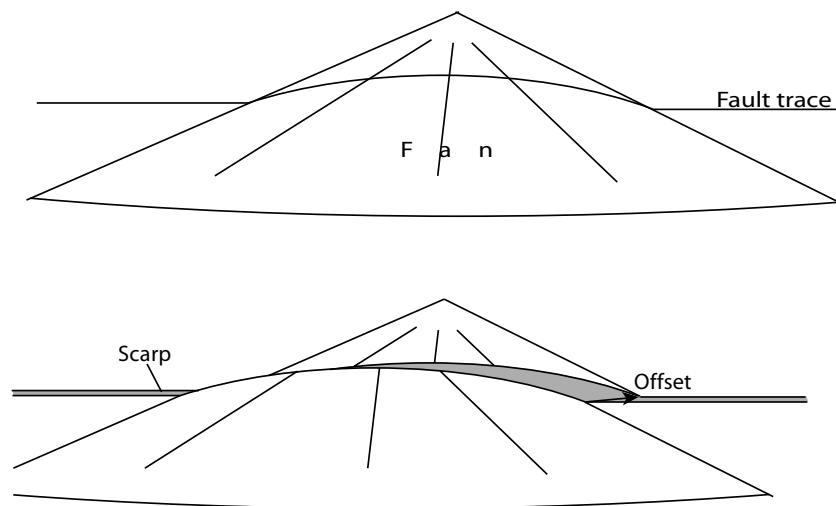


Figure 7. True observed offset where a fault cuts a fan (schematic front view). Indeed, the local slope can induce misfits in the calculation of vertical offsets (see Appendix C).

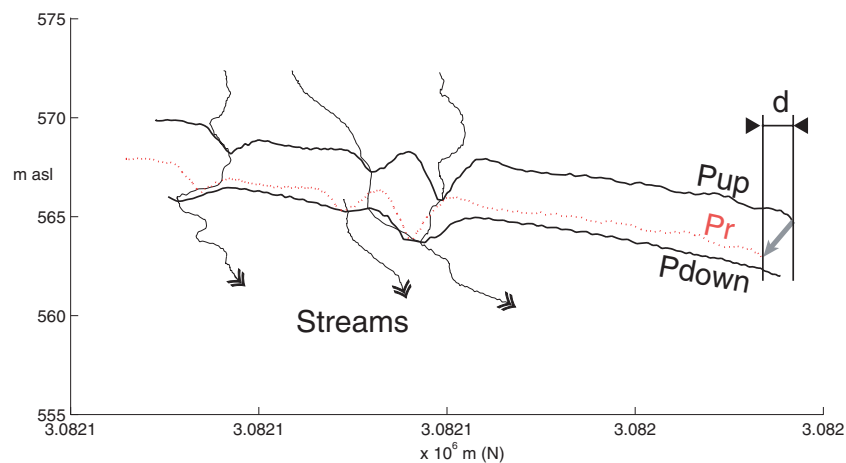


Figure 8. Graphical strike-slip offset measurement for site K01. The view is a projection into a vertical plane parallel to the fault trace; the abscissa is north–south with coordinates in metres in the UTM 40 North reference frame; the ordinate is the elevation, indicated in metres above sea level (m asl). Pup and Pdown are two observed profiles parallel to the fault trace, upstream and downstream to the fault, respectively. Pr is Pup restored to a possible initial position that fits the highs and lows of Pdown. The horizontal distance d between Pr and Pup represents the horizontal offset due to fault slip.

from both fan boundaries. In the absence of horizontal offset, the hangingwall and footwall medians should meet at a fault trace; otherwise, the distance between the meeting points of each median at the fault trace represents the offset (*cf.* Fig. 10c). Even if this method was successfully applied to some fans (Fig. 10c), it cannot be generalized to the studied area. This method indeed requires well-defined fan boundaries. Since fans are densely distributed in the studied area, their boundaries have often been perturbed. In addition, this method has to assume that the median is a straight line, implying a local slope perpendicular to the fault and to the relieves. In the studied area, the fans are mainly along the lateral slope of valleys and show an important curvature, which is incompatible with the preliminary assumption.

Average long-term slip rates along the faults were then estimated using the previously described Late Quaternary alluvial fan abandonment dating. Indeed, the observed cut and fill-in process emplacement strongly suggests that the offset channel networks of the different fan units were formed just after their abandonment. In such cases alluvial fans that are indicators of climatic changes may be

used not only as markers allowing identification of cumulative tectonic displacements through their offset streams, but also to directly estimate the horizontal displacement slip rate through the dating of the abandonment of the alluvial fan surface using *in situ*-produced ^{10}Be (e.g. Siame *et al.* 1997, 2001).

4 RESULTS: OFFSET FAULT SLIP RATES

We have investigated the major Minab, Zendan, Palami, Jiroft and Sabzevaran faults and the secondary Kahnij Fault (Fig. 2). Their surface trace usually consists of a discontinuously steep, fresh-looking scarp at the foot of relieves. The Zendan, Minab and secondary Kahnij faults are located west of the relief and are west facing (east-dipping fault planes), while the others are east-facing frontal faults associated with west-dipping faults (Fig. 2).

Offset measurement and site locations are presented Table 2 and Fig. 2, respectively. For convenience, the same site references as in Regard *et al.* (2004) were used, i.e. sites are presented from

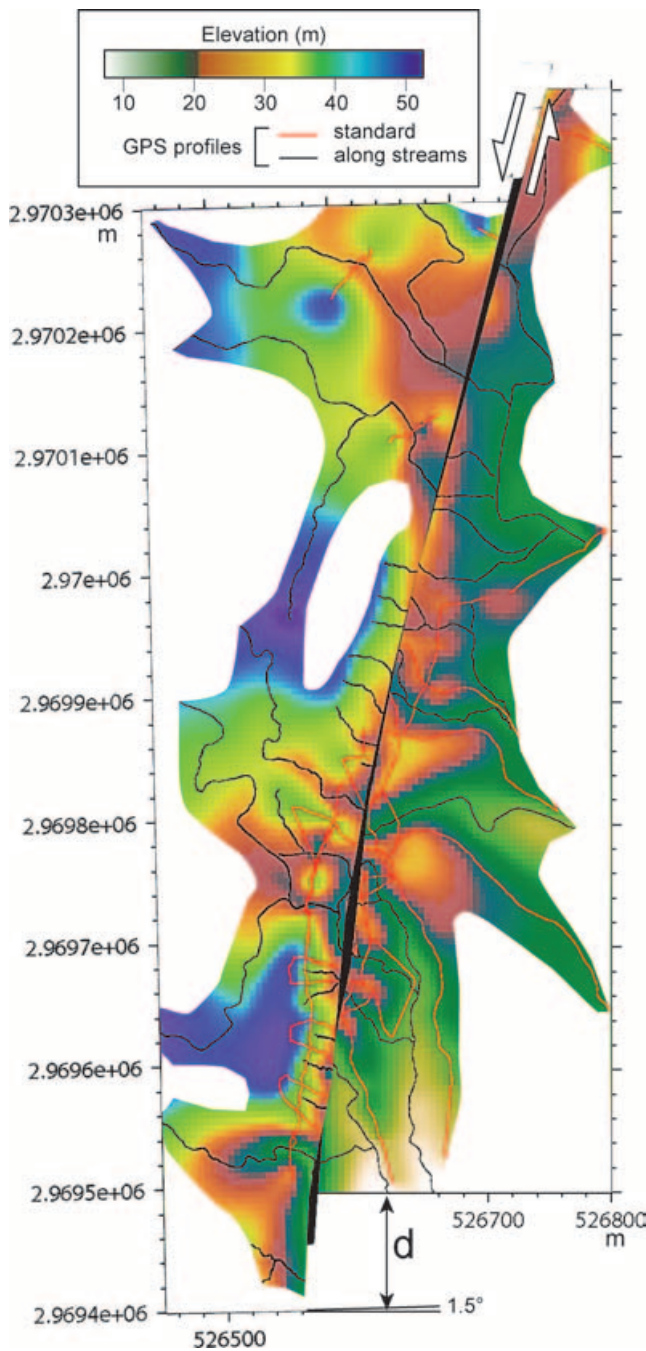


Figure 9. Digital elevation model (DEM) of location P02 and the offset estimate (d) of 94 m. Coordinates are in metres in the UTM 40 North reference. This DEM is generated after GPS measurements along red and black profiles (black profiles are stream profiles); elevation increases from white to brown then violet. Extrapolation was made by the *surface* function of GMT software (Wessel & Smith 1995) in order to produce a map suitable for the evaluation of offsets and correspondence between eastern and western parts. Pixel size is 5×5 m.

southwest to northeast and from that along the Minab Fault to those along the Zendan, Palami, Sabzevaran, Kahnuj and then Jiroft faults. Offset values and inferred ages of the displaced geomorphic features and abandonment surfaces of each along-strike fault site used to calculate the vertical-/lateral-component slip rate (lateral, column d_{ss} , and vertical, column d_v), are presented in Table 2. We assume that the vertical slip rates around our faults are not constant

along the fault, whereas the strike-slip velocities must be nearly constant.

In Table 2, the method used to determine the strike-slip displacements is specified. In addition, we report the relative displacement of the southwestern part with respect to the northeastern one and indicate its azimuth (Table 3), following the method detailed in Appendix B. Below we report results of offset measurement and deduced slip rate for significant localities along each fault zone constituting the Minab–Zendan and Jiroft–Sabzevaran fault systems.

4.1 Minab Fault

The Minab Fault zone is conspicuous along about 50 km and trends parallel to the coast of the Hormoz Strait with a $N160^\circ E$ mean strike (Fig. 2). It consists of a discontinuous and non-linear segment succession of 25° – 45° east-dipping thrust faults that affect the Late Cenozoic strata and the Quaternary deposits and it is closely associated with the Minab Fold and bounds it to the west. To the south, it obliquely cross-cuts the fold, while to the north the thrust splits into two distinct segments (Regard *et al.* 2004). The western segment corresponds to an east-dipping reverse fault affecting the Late Pleistocene fans at the front of the fold and thrust belt, while the eastern segment is an inactive northeast-dipping thrust that obliquely cross-cuts the Minab Fold.

Measurements were conducted at four sites along the Minab Fault north of Minab City, where the active fault trace is clearly underlined by a relatively continuous west-facing scarp affecting Quaternary surfaces. At these localities, slip-vector (striae) measurements on the fault plane provide evidence for a present-day nearly dip-slip motion with a small right-lateral component (the major faulting horizontal slip-vector strike is about $N45^\circ E$) (Regard *et al.* 2004).

The first site is located immediately south of the Karun River (site M05bis, $27^\circ 20.8' N/56^\circ 59.0' E$, Fig. 2) which has dissected the eastern and northern flanks of a relatively small remnant extension of a Qt_{1a} fan. The top surface of the fan is flat and the Minab Fault displaces its southwestern edge. The amplitude of three vertical offsets on the abandoned fan surface was measured by profiles perpendicular to the fault scarp established using differential GPS. At site M05bis, vertical offset averages 8.8 ± 0.3 m. As Qt_{1a} age in the western piedmont is 22.1 ± 1.6 ^{10}Be kyr (see above, Section 2.3), the vertical displacement rate is 0.40 ± 0.03 $mm\ yr^{-1}$. Knowledge of the fault geometry and kinematics allows us to calculate an average strike-slip rate of 0.15 ± 0.10 $mm\ yr^{-1}$ (Table 2).

Between this first site and the Karun River, a well-preserved Qt_2 fan surface (site M05) has been displaced by the Minab Fault. Five vertical offsets surveyed provide an average vertical offset of 2.3 ± 0.2 m. However, three values corresponding to well-preserved parts close to each other converge to a constrained vertical offset of 2.2 ± 0.1 m. ^{10}Be dating indicates for this surface an abandonment (location M05bis) 13.6 ± 1.1 ^{10}Be kyr ago (*cf.* Section 2.3). This leads to a vertical displacement rate of 0.16 ± 0.02 $mm\ yr^{-1}$ that is turned into a strike-slip rate of 0.10 ± 0.07 $mm\ yr^{-1}$ (Table 2).

The next site is localized along the Karun River (M06, $27^\circ 22' N/56^\circ 58' E$, Fig. 2). At this location, the surface morphology is complex due to numerous erosion and deposition phases. Consequently, it is difficult to follow and map the damaged fault scarp. To better locate the fault trace, we thus produced a DEM (Fig. 11) based on 20 measured topographic profiles (profiles perpendicular and parallel to the fault and along-strike streams through the fault trace). This allows us to determine a vertical offset of 0.7 ± 0.1 m. Since no abandonment age can be proposed for this surface due to

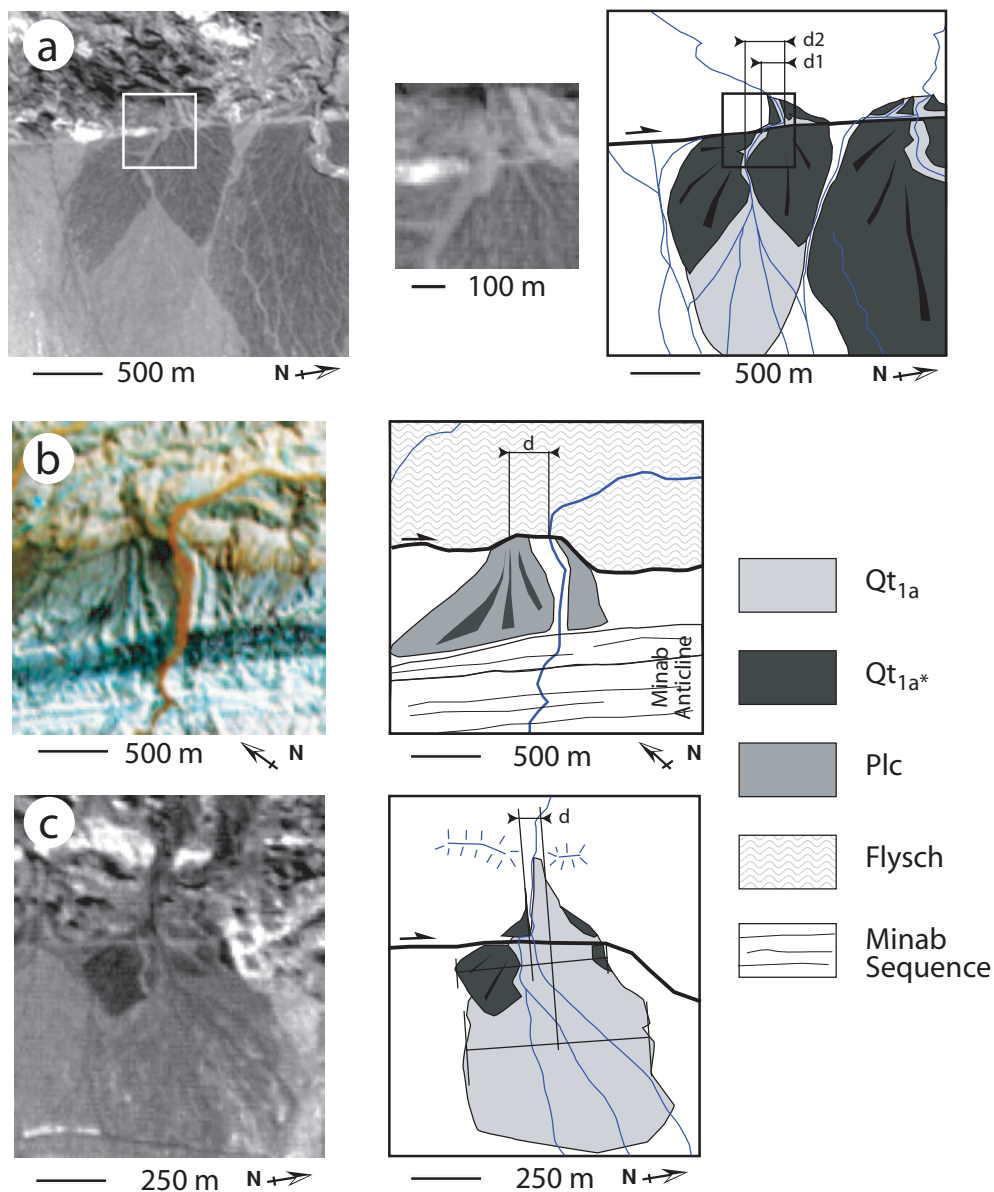


Figure 10. Different types of offsets measured on satellite images and aerial photographs. (a) Right-lateral stream offset on the Sabzevaran Fault. The stream emplacement occurred just after the Qt_{1a*} deposition. $d1$ and $d2$ represent two possible values of offset. We prefer $d1$ because it only represents an offset along the fault without internal fan deformation. They are respectively of about 150 and 300 m. (b) Right-lateral offset of stream and fan edge, along the Zendan Fault. The fan edge is the convergence point of little streams that developed within the fan. This point should indicate the former main stream emplacement. The offset, d , between this point and the current main stream is measured to 240, 310 or 390 m as a function of the uncertainties on the fan edge. The fan is Plc, after the Minab quadrangle map (McCall *et al.* 1985), but could be also of Qt_1 age. (c) Fan evidence of right-lateral motion. The median method is used: first, the envelope of the fan is drawn, then the line between the two lateral sides of the fan, and the median of this line. Finally, the distance between two medians is measured along the fault trace. Generally these two medians are the upstream and downstream medians of the same offset fan. Here the method is applied with two generations of fans, the first one being offset with respect to the second one. This offset, d , is thought to indicate the right-lateral motion on the Sabzevaran Fault between the two deposition stages. This offset evaluation ranges from 56–81 m.

the significant inheritance and complex surface history no slip rate can be provided (Table 2).

North of the Karun River, the geomorphic surface offset of remnant alluvial deposits (Qt_{1a} and Qt_2 ; site M07 at $27^{\circ}22.2'N/56^{\circ}57.5'E$, Fig. 2) lying between two secondary streams of the major river was studied. Since they incised the alluvial deposit surface, minor streams displaced by the fault activity developed after emplacement of the alluvial deposit and abandonment of the related surface. Nine fan surface topographic profiles, measured by differ-

ential GPS across the fault scarp, provide evidence for vertical fault offsets ranging from 1.6 to 3.6 m. Considering the data distribution, an average value, computed from seven out of the nine measurements, gives a vertical offset of 2.0 ± 0.2 m. (This site is considered in detail in Appendix D to show the way in which we calculate site offsets.) A graphical method applied over the general mapping of the site indicates a possible right-lateral offset of ~ 23 m. This is significantly higher than the 0.7 ± 0.5 m horizontal offset implied by a vertical offset of 2 m when considering the azimuth ($N140^{\circ}E$),

Table 2. The evidence for strike-slip velocities. Vertical offsets (dv) are translated into strike-slip offsets (dss) or inversely, thanks to the striae data (azimuth, dip and pitch of the fault plane). We calculate the horizontal displacement associated with dv or dss , in terms of total horizontal displacement dH , northward displacement dN , eastward displacement dE , and azimuth Az (see Fig. A1). The estimated ages of the geological objects offset are indicated. There are two or three ages for each offset. These ages are estimated from regional correlations except those for which there are more direct ^{10}Be age determinations, indicated in bold type. Strike-slip velocities are shown (vss). They are in bold type when they are directly calculated from lateral offsets and not inferred from vertical offsets. The error bars indicated are 66 per cent confidence error bars, and we assume for dv an additional 10 cm error induced by GPS measurements.

Fault	Location	Fault plane			Meas. dv		Ded. dss	Meas. dss	Ded. dv	Horizontal displacement			Age	vss (mm yr $^{-1}$)	vv (mm yr $^{-1}$)	Mean vss (mm yr $^{-1}$)
		Az	Dip	Pitch	(m)	(m)				dH (m)	dN (m)	dE (m)				
Minab	M05-bis	320(±5)	45(±5)	75(±10)	8.80(±0.32)	3.33(±2.22)		9.41(±1.85)	29.2(±21.3)	22100(±1584)	0.15(±0.101)	0.398 (±0.032)				
	M05	325(±5)	25(±5)	75(±10)	2.20(±0.13)	1.39(±0.95)		4.92(±0.47)	38.5(±17.8)	13618 (±1123)	0.102(±0.070)	0.162 (±0.016)				
	M06	320(±5)	32(±5)	75(±10)	0.66(±0.10)	0.33(±0.23)		1.10(±0.15)	32.5(±19.1)							
	M07	320(±5)	45(±5)	75(±10)	1.98(±0.21)	0.75(±0.50)		2.12(±0.48)	29.2(±22.2)	5724(±633)	0.131(±0.089)	0.346 (±0.053)			0.128(±0.087)	
Zendan	Between Z07 and Z08	340(±5)	60(±10)	40(±10)			86.25(±14.06)	62.68(±21.41)	119.90(±50.82)	178.93(±60.20)	2.8(±17.9)	42000(±4200)	3.93 (±0.60)		3.92(±0.68)	
	(satellite)	340(±5)	60(±10)	40(±10)	313.33(±50.89)	227.69(±99.93)	339.79(±129.68)	2.8(±18.5)	80000(±8000)	3.92(±0.75)						
	Id*	340(±5)	60(±10)	40(±10)	86.25(±14.06)	62.68(±27.52)	93.53(±35.75)	2.8(±18.5)	42000(±4200)	2.05 (±0.39)					2.24(±0.40)	
		340(±5)	60(±10)	40(±10)	165.00(±19.08)	119.90(±50.82)	178.93(±60.20)	2.8(±17.9)	80000(±8000)	2.06 (±0.32)						
Palami	P02	185(±5)	80(±5)	4.5(±10)	15.69(±0.48)	1.22(±2.76)		15.69(±0.70)	5.8(±6.8)	9223(±971)	1.70(±0.19)	1.70 (±0.19)				
		185(±5)	80(±5)	4.5(±10)	27.87(±1.50)	2.16(±4.91)		27.87(±1.89)	5.8(±6.8)	13618(±1123)	2.05 (±0.20)					
		185(±5)	80(±5)	4.5(±10)	53.00(±1.00)	4.11(±9.33)		53.00(±1.74)	5.8(±6.8)	22100(±1584)	2.40 (±0.18)					
		185(±5)	80(±5)	4.5(±10)	94.00(±1.00)	7.29(±16.56)		94.01(±2.31)	5.8(±6.8)	42000(±4200)	2.24 (±0.23)				2.09(±0.27)	
P04	180(±5)	75(±5)	12.3(±10)	113.00(±8.48)	23.80(±20.67)		113.18(±13.11)	3.2(±8.0)	42000(±4200)	2.69 (±0.34)						
P07	155(±5)	55(±5)	38(±10)	8.81(±0.64)	13.77(±4.20)		15.08(±4.64)	-0.9(±13.6)	9223(±971)	1.49(±0.48)	0.96 (±0.12)					
Middle plain	P08	138(±5)	38(±10)	-80(±10)	-16.36(±0.60)	4.69(±4.80)		21.46(±4.35)	60.6(±20.5)	22100(±1584)	0.21(±0.22)	-0.74 (±0.06)				
Middle plain-2	P08	120(±5)	45(±10)	-75(±10)	-24.80(±0.10)	9.40(±6.56)		26.52(±8.05)	50.8(±26.8)	42000(±4200)	0.22(±0.16)	-0.59 (±0.06)				
Sabzevaran	S03	177(±5)	78(±5)	14(±10)	3.60(±0.18)	14.76(±12.02)		14.78(±12.37)	-0.0(±7.7)	5724 (±633)	2.58(±2.12)	0.63 (±0.08)				
		177(±5)	78(±5)	14(±10)			11.70(±0.55)	2.85(±2.32)		5724 (±633)	2.04 (±0.25)	0.50(±0.41)				
		177(±5)	78(±5)	14(±10)			76.95(±5.10)	18.77(±15.31)		22100(±1584)	3.48 (±0.34)	0.85(±0.70)				
		177(±5)	78(±5)	14(±10)			144.00(±0.00)	35.12(±28.55)		42000(±4200)	3.43 (±0.34)	0.84(±0.68)				
Kahnuj1	S02	177(±5)	78(±5)	14(±10)			65.00(±13.03)	15.85(±13.27)		22100(±1584)	2.94 (±0.63)	0.72(±0.60)				
	Satellite	177(±5)	78(±5)	14(±10)			143.50(±16.47)	35.00(±28.73)		42000(±4200)	3.42 (±0.52)	0.83(±0.69)				
		177(±5)	78(±5)	14(±10)			59.25(±14.74)	14.45(±12.28)		19900(±5784)	2.98 (±1.14)	0.73(±0.65)				
		5(±5)	60(±10)	18(±10)	2.72(±0.15)	9.65(±6.08)		9.78(±6.24)	14.2(±17.5)	5724(±633)	1.69(±1.08)	0.47 (±0.06)				
Kahnuj2	K01	5(±5)	60(±10)	18(±10)			7.94(±0.42)	2.23(±1.41)		5724(±633)	1.39 (±0.17)	0.39(±0.25)		1.54(±0.62)		
	as for Kahnuj1	5(±5)	60(±10)	18(±10)	1.36(±0.13)	4.83(±3.07)		4.90(±3.15)	14.2(±11.8)	5724(±633)	0.84(±0.54)	0.24 (±0.03)				
Jiroft	SPT	183(±5)	52(±10)	24(±10)			3.98(±0.49)	1.12(±0.71)		5724(±633)	0.69 (±0.11)	0.20(±0.13)		0.77(±0.33)		
		183(±5)	52(±10)	24(±10)			48.75(±17.20)	17.10(±10.16)		22100(±1584)	2.21(±0.79)	0.77(±0.46)				
		183(±5)	52(±10)	24(±10)			133.17(±17.97)	46.72(±23.19)		42000(±4200)	3.17(±0.53)	1.11(±0.56)		2.69(±0.66)		

*For the Sabzevaran fault, due to multiple estimates, we show here the two solutions we found.

Table 3. Horizontal motion of the southwestern block with respect to the northeastern block, deduced from the fault slip rates; errors are 66 per cent confidence intervals. v_{SS} is the strike-slip rate of the fault deduced from Table 1 and vv is the deduced vertical velocity. From these velocities we deduce the motion of the southwestern block with respect to the northeastern block (vh) that can be divided into northward (dN) and eastward (dE). We also deduced the motion within the fault plane (vs) (see Fig. 10 to visualize the different offsets and related motions). Two cases, a and b, are distinguished for the Zendan Fault (see text). Different evaluations, as a function of the fault plane parameters, are represented for the Minab and Zendan faults; the average value used in text is indicated. The sum of the motions on each fault system (Minab–Zendan and Jiroft–Sabzevaran) is calculated. For the Jiroft–Sabzevaran we assume the Kahnuj Fault as a segment of the Sabzevaran Fault (±see text) and we do not add its motion to that of Sabzevaran Fault. Finally, the motion of the Musandam Peninsula with respect to the Jaz Murian is quantified by the faults to 11.2 ± 3.9 or 13.0 ± 4.3 mm yr⁻¹ in a direction, respectively, N11 ± 19°E and N10 ± 19°E.

Fault	Fault plane			v_{SS} (mm yr ⁻¹)	Ded. vv (mm yr ⁻¹)	vh (mm yr ⁻¹)	Total velocity (geographic)			vs (mm yr ⁻¹)
	Az	Dip	Pitch				dN (mm yr ⁻¹)	dE (mm yr ⁻¹)	Az (deg)	
Minab	320(±5)	45(±5)	75(±10)	0.13(±0.09)	0.34(±0.32)	0.36(±0.33)	0.32(±0.31)	0.18(±0.23)	29.2(±50.1)	0.49(±0.46)
	325(±5)	25(±5)	75(±10)	0.13(±0.09)	0.20(±0.19)	0.45(±0.43)	0.35(±0.36)	0.28(±0.31)	38.5(±57.8)	0.49(±0.47)
	320(±5)	32(±5)	75(±10)	0.13(±0.09)	0.25(±0.24)	0.43(±0.40)	0.36(±0.35)	0.23(±0.27)	32.5(±52.0)	0.49(±0.47)
<i>Mean</i>						<i>0.34(±0.34)</i>	<i>0.23(±0.27)</i>	<i>33.4(±53.3)</i>	<i>0.495(±0.47)</i>	
Zendan	a	60(±10)	40(±10)	3.92(±0.68)	2.85(±1.26)	4.25(±0.97)	4.24(±0.98)	0.20(±1.38)	2.8(±18.6)	5.11(±1.48)
	b	60(±10)	40(±10)	2.24(±0.40)	1.63(±0.73)	2.43(±0.57)	2.43(±0.57)	0.12(±0.79)	2.8(±18.7)	2.93(±0.86)
Palami		80(±5)	4.5(±10)	2.09(±0.27)	0.16(±0.37)	2.09(±0.27)	2.08(±0.27)	0.21(±0.25)	5.8(±6.9)	2.10(±0.30)
		180(±5)	75(±5)	2.09(±0.27)	0.44(±0.39)	2.10(±0.27)	2.09(±0.27)	0.12(±0.29)	3.2(±8.1)	2.14(±0.35)
		155(±5)	55(±5)	2.09(±0.27)	1.34(±0.43)	2.30(±0.38)	2.29(±0.38)	-0.03(±0.58)	-0.9(±14.4)	2.66(±0.54)
<i>Mean</i>						<i>2.16(±0.37)</i>	<i>0.10(±0.37)</i>	<i>2.7(±9.8)</i>	<i>2.301(±0.40)</i>	
Middle plain		38(±10)	-80(±10)	0.21(±0.22)	-0.74(±1.07)	0.97(±1.41)	0.48(±0.81)	0.85(±1.25)	60.6(±69.1)	1.22(±1.78)
Middle plain-2		45(±10)	-75(±10)	0.22(±0.16)	-0.59(±0.59)	0.63(±0.62)	0.40(±0.48)	0.49(±0.53)	50.8(±62.7)	0.71(±1.04)
Total Minab–Zendan fault system	a			6.35		7.35(±2.68)	7.22(±2.16)	1.38(±3.00)	10.8(±24.0)	
	b			4.68		5.56(±2.26)	5.41(±1.75)	1.29(±2.41)	13.4(±25.9)	
Sabzevaran		78(±5)	14(±10)	2.98(±0.76)	0.73(±0.62)	2.99(±0.77)	2.99(±0.77)	0.00(±0.41)	0.0(±7.9)	3.07(±0.89)
Kahnuj		60(±10)	18(±10)	2.31(±0.95)	0.65(±0.49)	2.34(±0.99)	2.26(±0.97)	0.57(±0.59)	14.2(±16.1)	2.42(±1.08)
Jiroft		52(±10)	24(±10)	2.69(±0.66)	0.94(±0.51)	2.79(±0.76)	2.65(±0.75)	0.88(±0.74)	18.3(±16.8)	2.94(±0.88)
Total Jiroft–Sabzevaran fault system				5.67		5.70(±1.68)	5.63(±1.52)	0.87(±1.15)	8.8(±11.9)	
Total	a					13.05(±4.34)	12.85(±3.68)	2.25(±4.15)	9.9(±18.7)	
Total	b					11.25(±3.90)	11.04(±3.27)	2.17(±3.56)	11.1(±18.8)	

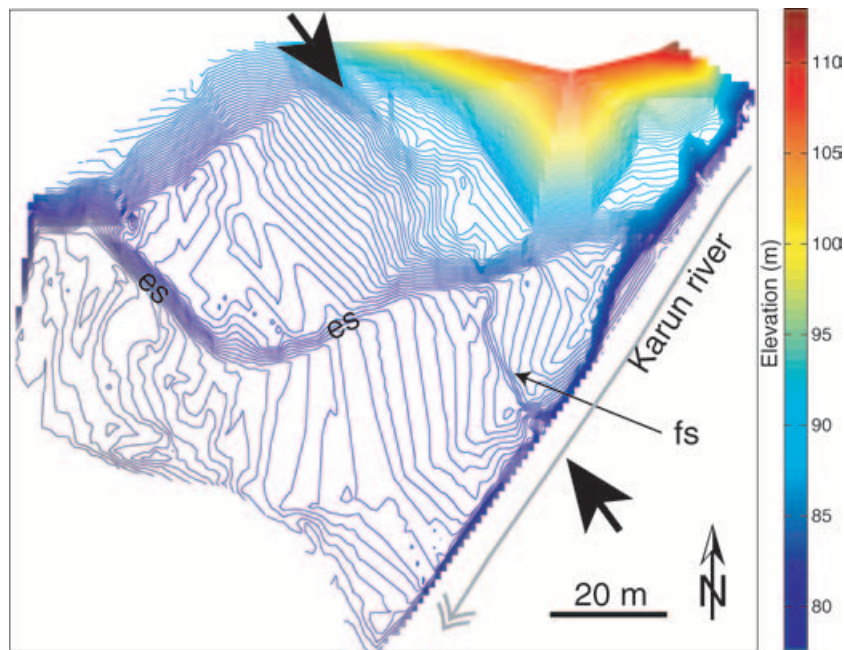


Figure 11. Contour map of a digital elevation model (DEM) of site M06 which permits us to differentiate scarps of erosional origin (es) from those of tectonic origin (fs); elevation increases from violet to red. Large arrows indicate the deduced Minab fault trace. The DEM is interpolated from 2-D profiles by the *griddata* function of Matlab software, with a linear extrapolation method that smooths the data: as a consequence the scarps observed are underestimated: every scarp observed on this DEM thus corresponds to something real in nature, not an artefact.

the dip (32°E) and the pitch (75°N) of the fault plane. Qt_2 fan surface abandonment was dated by regional geomorphic correlation at 5.7 ± 0.6 ^{10}Be kyr; this leads to a vertical slip rate estimate of 0.35 ± 0.05 mm yr^{-1} , and then to a strike-slip rate of 0.13 ± 0.09 mm yr^{-1} (Table 2).

In summary, geomorphic evidence for displacement along the Minab Fault indicates that this fault-strike average slip rate is 0.13 ± 0.09 mm yr^{-1} (Table 2). These values yield an average horizontal motion velocity of one side of the fault with respect to the other side of the fault of 0.13 ± 0.09 mm yr^{-1} , its azimuth being around $\text{N}33 \pm 53^{\circ}\text{E}$ (average value, Table 3); the fault corresponds to a nearly pure thrust.

4.2 Zendan Fault

The NNW-trending, east-dipping, Zendan Fault represents the main lithological boundary between the Zagros and the Makran (Fig. 2). It is a roughly 250 km long oblique reverse-lateral fault going from the MZT to the north, to the Gulf of Oman to the south. The Zendan Fault is highly segmented and it is arranged in *en echelon* segments, along the northernmost 50 km.

The central part of the fault zone is characterized by relatively continuous traces locally highlighted by a west-facing scarp within the Quaternary deposits. However, places where offset measurements are possible along the Zendan Fault are rare and virtually inaccessible. Consequently, fault offset measurements and deduced slip rates are limited to three sites.

The first site (Z04, $26^{\circ}55'\text{N}/57^{\circ}15'\text{E}$, Fig. 2) corresponds to a fan (Qt_2) whose abandonment surface, partly reworked, presents a west-facing scarp. Since the fan shape is not well preserved, vertical offsets deduced from profiles perpendicular to the fault scarp using differential GPS are scattered. They give an average vertical offset of 1.7 ± 0.1 m.

The second site (Z09, $27^{\circ}24.9'\text{N}/57^{\circ}00.8'\text{E}$, Fig. 2) corresponds to a fan made up of coarse material (Qt_{2a}). Surveying the morphology of the surface by profiles normal to the fault scarp provides vertical offsets whose estimates range from 1.2 to 3.7 m (mean 2.4 ± 0.4 m). The large dispersion of data is due to surface degradation; the maximum vertical offset is probably representative of the cumulative faulting displacement.

The third studied site (Z09bis, $27^{\circ}25.2'\text{N}/57^{\circ}00.8'\text{E}$, Fig. 2) is of slightly better quality than the second one. It corresponds to a recent fan, whose deposition is probably contemporaneous with Qt_{2a} deposits. A fault scarp crosses the fan. Seven selected GPS profiles perpendicular to it, out of a total number of eight, indicate a vertical offset of 1.3 ± 0.1 m.

These three sites do not provide robust constraints for an accurate estimate of vertical offset, and, consequently, of horizontal slip rates. An alternative approach for quantification is SPOT image analysis. To constrain the long-term slip rate of the fault detailed mapping of the active fault traces and of the along-strike offsets has been performed using SPOT images. This permits us to determine a horizontal long-term slip rate on the fault, at the Late Pleistocene timescale, by observations of stream offsets. Along the Zendan Fault trace (south of the two latter sites, near $27^{\circ}30'\text{N}/57^{\circ}10'\text{E}$), they are right-laterally offset, the offset values being distributed around three mean values of 86, 165 and 313 m (Table 4). Unfortunately, these offsets were measured in remote areas. Dating is thus attempted by correlation with the time succession of deposits as previously described.

The 86 m mean offsets are undoubtedly associated with the most recent of the studied deposits and the 313 m mean offsets are associated with deposits mapped as Plc. Based on previous analysis of the regional climate variations (Regard 2003; Regard *et al.* 2004), this implies that the sequence of deposition is either 22.1 ± 1.6 ^{10}Be kyr, 42 ± 4.2 kyr BP and 80 ± 8 kyr BP, or 42 ± 4.2 , 80 ± 8 and

Table 4. Evidence of offsets along the Zendan, Sabzevaran and Jiroft faults as deduced from satellite images. Observed offsets are indicated in metres. Types of measurements can be stream or fan offsets, offset between the edge of the fan or the median of the fan and the main stream of the fan (see text and Fig. 10).

Fault	Location	Observed offsets	Type	Age	Mean offset	Std dev.
Zendan	~27°30'N, 57°10'E	80	Stream	Qt ₂	86.2	9.5
		80	Stream			
		85	Stream			
		100	Stream			
		145	Stream			
		175	Stream			
		175	Stream			
Sabzevaran	~27°47'N, 57°40'E	240–310–390 (b)	Stream–fan edge	Plc ^a	313.3	75.6
		30 ^b	Stream	Qt _{1a*}		
		50–85	Stream			
		50–80	Stream–fan			
		50	Fan–fan	Amount of time		
		56–81 (c)	Fan–fan	between Qt _{1a*} and Qt _{1a} ^c		
		150 or 300 ^b (a)	Stream	Qt _{1a} + (Qt _{1a*} – Qt _{1a}) ^c		
Jiroft	~27°35'N, 57°48'E	112–137–162	Stream–fan edge	Qt _{1a}	124.2	29.8
		25–70	Fan	Qt _{1a*}		
		50	Stream–fan			
		125	Fan			
		95	Fan			
		100–137–187	Stream–fan edge			
		100–125–150	Stream			

^aPlc, after the Minab geological map (McCall *et al.* 1985) or younger, may be Qt₁.

^bItalic numbers are low-confidence measurements.

^cThe offset between two fans generations is thought to indicate the total offset between the two deposition stages Qt_{1a} and Qt₂; thus adding this offset with the offset since the last deposition stage (Qt₂) gives the total offset since the first deposition stage Qt_{1a}.

Labels (a), (b) and (c) refer to parts of Fig. 10.

120 ± 12 kyr BP. Depending on the chosen sequence, this leads to values of strike-slip rates ranging either between 3.9 ± 0.7 mm yr⁻¹ or 2.2 ± 0.4 mm yr⁻¹. We discard periods of 9.2, 13.6, 65–70, 180–210 and 300–325 kyr BP, the first two because they imply a young age incompatible with the fan surface signature on satellite images (colour, position relative to other fans). The others have been discarded because we cannot arrive at coherent values, on the contrary to the chosen sequences that leads to closely distributed values.

Due to the rough relief and the lack of sites where the Zendan Fault crosses Quaternary deposits, it has not been possible to discriminate between mean values of strike-slip rate of 3.9 ± 0.7 and 2.2 ± 0.4 mm yr⁻¹. The azimuth of the associated displacement is N3 ± 19°E (Table 3).

4.3 Palami Fault

The Palami Fault is an oblique reverse-lateral slip fault nearly parallel and similar to the Zendan Fault. To the north, near the MZT, it is not conspicuous. Near Minab it is located 5 km east of the Zendan Fault, while to the south it is 20 km away from the Zendan Fault. The Palami Fault is a high-angle west-dipping fault, whose trace is all along-strike underlined by east-facing scarps affecting Quaternary fans. The Palami Fault was investigated at three sites. In addition, we studied two sites on fault traces that split southeastwards from the Palami Fault.

First, near Geru (location P02, 26°50.8'N/57°15.9'E, Fig. 2), we mapped, again using differential GPS, streams incised in Qt₂ deposits (as mapped by McCall *et al.* 1985) and the associated crests, both being horizontally displaced by the fault. Forty-eight GPS profiles, the majority corresponding to crest and streams, allow the generation of a local DEM that covers an area of 400 × 900 m (Fig. 9). Graphic correspondence between upstream and downstream areas of the DEM, as well as between upstream and downstream chan-

nels, demonstrates four right-lateral offsets. The lowest river stream offsets measured using differential GPS indicate consistent values of 15.7 ± 0.5 m (six measurements) and 27.9 ± 1.5 m (five measurements). The best explanation for them is a minor reorganization of drainage following pluvial or tectonic events. The highest offsets correspond to two possible offset values since the Qt₂ surface abandonment. These are 53 m and 94 m with an associated uncertainty of the order of 1 m. All these offsets are associated with the end of wet periods on the basis of regional correlation at 9.2 ± 1.0 ¹⁰Be kyr (Holocene in the eastern domain of the study area), 13.6 ± 1.1 ¹⁰Be kyr (epi-Palaeolithic), 22.1 ± 1.6 ¹⁰Be kyr BP and 42.0 ± 4.2 ¹⁰Be kyr, respectively. The strike-slip rates calculated are respectively 1.7 ± 0.2, 2.0 ± 0.2, 2.4 ± 0.2 and 2.2 ± 0.2 mm yr⁻¹ (Table 2).

Farther north, to the southeast of the Palami Mountains, the site P04 (27.08°N, 57.28°E, Fig. 2) displays an interesting feature of stream offsets that provide evidence for a 113 ± 8 m horizontal displacement on the fault (*cf.* Fig. 12), measured on aerial photographs. After geological mapping (McCall *et al.* 1985), the deposits are Qt_{1a}, i.e. dated at 42.0 ± 4.2 ¹⁰Be kyr. The deduced strike-slip rate is thus 2.7 ± 0.3 mm yr⁻¹ (Table 2).

To the northeast of the Palami Mountains, at Dast Kerd village (P07, 27°08.8'N/57°15.2'E, Fig. 2), an important fault scarp, affecting a Quaternary fan, has an height, measured by differential GPS, of 8.8 ± 0.6 m. Note that in spite of the number of measurements (seven) the standard deviation is important. However, this mean value is considered as valuable, since these seven profiles are carefully selected from 11 on the basis of their freshness. ¹⁰Be ages indicate an abandonment of this surface at 9.2 ± 1.0 ¹⁰Be kyr. This leads, using fault kinematics, to a strike-slip rate of 1.5 ± 0.5 mm yr⁻¹ (Table 2).

Northeast of Dast Kerd, two scarps are found on two faults linked to the Palami Fault. They are situated within a plain containing deposits coming from Palami Mountain. The first scarp (Middle

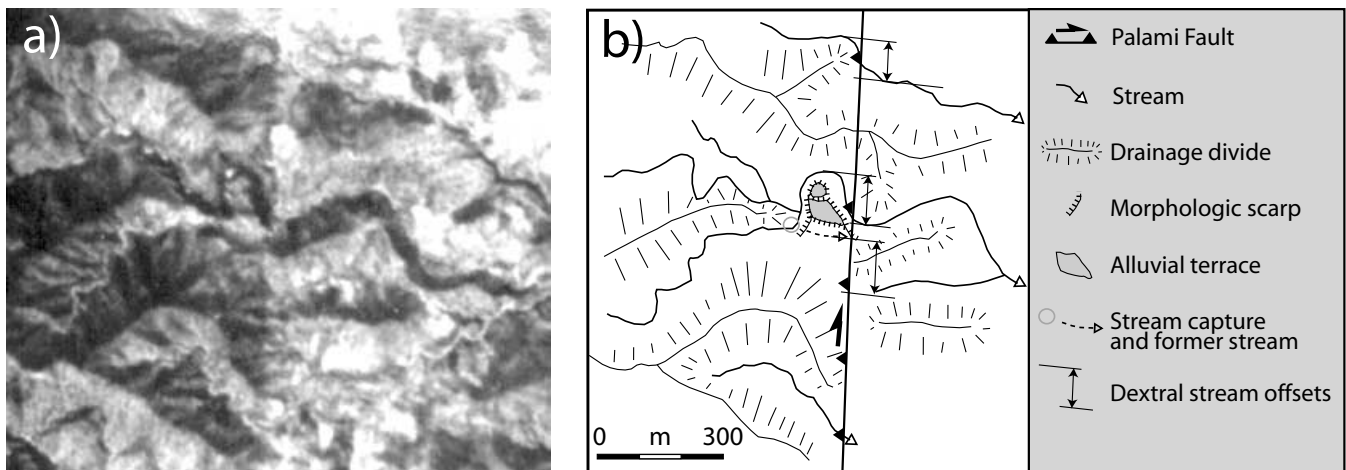


Figure 12. Aerial photograph of location P04 and its interpretative sketch, up to the north. The fault delimits the Palami mountain to the west and the Jaghin plain to the east.

Plain-1, P08, Fig. 2) within Qt_{1a} deposits is 16.4 ± 0.6 m high. This value results from four well-defined differential GPS profiles perpendicular to the scarp, to which we can add two others, of lesser quality, without significantly changing the average value (16.0 ± 0.4 m). The second scarp (Middle Plain-2) is not so well preserved and may also be within Qt_{1a} deposits. A single measurement indicates a vertical offset of ~ 25 m (low-confidence). Taking into account regional correlation and assuming that these faults are still active nowadays, we infer strike-slip rates for these two faults of the order of 0.21 and 0.22 mm yr^{-1} , respectively (Table 2). In fact, if Middle Plain-1 belongs to an apparently active fault, this may not be the case for Middle Plain-2, since it looks more like a hill alignment than a fault scarp. Note that the displacements associated with these two faults are oblique with respect to that of the Palami Fault. Their azimuths lie at around $N50$ – $N60^\circ\text{E}$ (70° confident, Table 3).

In summary, these assumptions lead to an estimate of the mean strike-slip rate of the Palami Fault (without any contribution from the Middle Plain faults) of 2.1 ± 0.3 mm yr^{-1} , the associated direction of motion being around $N3 \pm 10^\circ\text{E}$ (Table 3).

4.4 Sabzevaran and Kahnuj faults

The north-trending Sabzevaran Fault is along the western front of the 600 m elevation Zamin Band–Bargah valley whose trace is particularly well expressed and associated with morphological features such as faceted spurs, tectonic ridges, horizontal stream offsets, al-

luvial fan asymmetries or displacements at the base of the relief (Fig. 2). This and the linear characteristics of the fault trace suggest a closely vertical fault plane (i.e. about 80°W) and a main strike-slip faulting for its recent activity. However, geomorphic features as well as fault slip-vector (striae) measurements all along the fault provide evidence for recent strike-slip faulting with a small but significant reverse component (Regard *et al.* 2004). The Sabzevaran Fault also exhibits a fresh north-trending east-facing scarp over 30 km all along the road to Bandar Abbas, south of Kahnuj. It marks the foot of the frontal escarpment characterizing the eastern boundary of the 1500 m elevation Gireh Mountains, at the west of the 600 m elevation Zamin Band–Bargah valley. Consequently, the Sabzevaran Fault delimits two morphological domains: the mountainous domain characterized by a deeply incised drainage network and sharp mountain flanks, and the alluvial plain dipping gently 10° eastwards. The alluvial fans, localized within the alluvial plain, correspond to gently sloping, fan-shaped landforms created over time by the deposition of clastic sediments. They have been studied using combined cartography and geomorphic (SPOT and field) analyses. North of the Zamin Band–Bargah valley, the Sabzevaran Fault is relayed by the north-trending Kahnuj Fault underlined by west-facing scarp along the eastern valley side (Fig. 13). We found seven sites displaying clear stream or fan offsets (Fig. 13 and Table 2).

The first site, a well-preserved conic-shaped fan surface, is located near the road to Deh (S03, $27^\circ 42.0'\text{N}/57^\circ 38.2'\text{E}$, Fig. 2). Vertical offsets at the fault scarp obtained using differential GPS profiles



Figure 13. Photograph of the Sabzevaran Fault (see Fig. 2 for location). The fault scarp is clear and is outlined by black arrows. It offsets the fan surface (vertical offset of about 5 m). Note that higher surfaces are cut by the fault.

range from 2.3 to 3.7 m. A careful check of the different profiles shows that maximum and minimum values correspond to parts of the fan which are not well preserved. The four remaining profiles give a vertical offset of 2.9 ± 0.1 m. However, as the conical shape induces systematic error, a geometrical method giving both the strike-slip and dip-slip displacements was applied (see Appendix C). From six selected profiles for site S03, a lateral displacement of 16.1 ± 8.3 m and a vertical offset of 3.7 ± 0.6 m were deduced. Since this method requires subjective selection of the data and has large uncertainties (50 per cent) on strike-slip offsets deduced from vertical ones when the striae pitch angle is small (see for example Table 2), it was complemented by a graphical method (Fig. 8) that gives a lateral displacement of 10.6 to 12.8 m, in agreement with the previous estimate. This first site fan is assigned to Qt_{2*} thanks to its mapping by McCall *et al.* (1985) and ^{10}Be ages of pebbles from its surface. It is dated at 5.7 ± 0.6 ^{10}Be kyr. This evidence implies a local strike-slip rate of 2.6 ± 2.1 mm yr $^{-1}$ using the vertical offset, or of 2.04 ± 0.25 mm yr $^{-1}$ from the graphical method (Table 2).

For the Sabzevaran Fault, the uncertainties on the fault dip angle generate strike-slip offset with uncertainties which are too large to yield robust offset estimates. Thus, offset measurement methods other than GPS profiles were used in the other sites studied along this fault (Table 2).

At site S02 ($27^{\circ}47'N/57^{\circ}39'E$, Figs 2 and 4), the fault cross-cuts a 'black' (on satellite imagery) fan and offsets by 77 ± 5 m (along-stream differential GPS) two rivers that incise this fan. After ^{10}Be exposure dating, this fan was found to belong to the Qt_{1a} deposit level, whose age of surface abandonment is 22.1 ± 1.6 ^{10}Be kyr (*cf.* Section 2.3), leading to a strike-slip rate of 3.5 ± 0.3 mm yr $^{-1}$ (Table 2).

At the same site, a river offset of 144 ± 2 m is measured on a 'black' fan probably emplaced during the previous wet episode (Qt_{1a*}), regionally dated at 42.0 ± 4.2 kyr (*cf.* above). This yields an average slip rate of 3.4 ± 0.3 mm yr $^{-1}$ (Table 2).

Additionally, SPOT image analyses were performed to define the fan envelope of the generation of each fan and to determine the offsets within these fan envelopes (Fig. 10). Three measurements indicate a mean horizontal offset of 65 ± 8 m related to Qt_{1a} fans, and two other measurements a mean offset of 143 ± 12 m related to Qt_{1a} fans (Table 4). Two additional offsets indicating a right-lateral motion of 59 ± 10 m characterize the time interval between the deposition of Qt_{1a*} and Qt_{1a} fans. The sum of the offset accumulated during the time period between deposition of Qt_{1a*} and Qt_{1a} fans and of the offset since deposition of Qt_{1a} fans is 124 ± 18 m, in agreement with the value of 143 ± 12 m found for the total offset since deposition of Qt_{1a} fans. Regional correlation sets abandonment of the generation of black Qt_{1a*} fans at 42.0 ± 4.2 kyr and Qt_{1a} at 22.1 ± 1.6 ^{10}Be kyr (see above). This leads to mean strike-slip rates of, respectively, 3.4 ± 0.5 and 2.9 ± 0.6 mm yr $^{-1}$. The interval between the deposition of Qt_{1a*} and Qt_{1a} fans lasted for 19.9 ± 5.8 kyr; a third estimate for the fault strike-slip rate is 3.0 ± 1.1 mm yr $^{-1}$ (*cf.* Table 2).

In summary, these data indicate a mean strike-slip rate for the Sabzevaran Fault of 3.0 ± 0.8 mm yr $^{-1}$, with an associated displacement directed northwards ($\pm N8^{\circ}E$, *cf.* Tables 2 and 3).

The sole measurements site on the Kahnuj Fault exhibits two scarps on a relatively well-preserved light grey-coloured fan (K01, $27^{\circ}51.6'N/57^{\circ}40.8'E$, Fig. 2). Their vertical offsets measured using differential GPS are 2.8 ± 0.1 m (four values) and 1.4 ± 0.1 m (two values). The lower scarp offsets streams (Fig. 14). Geographical differential GPS profiles indicate horizontal offsets ranging from 6

to 12 m while evaluations using graphical analysis range from 4.1 to 7.8 m. Out of these GPS profiles and graphical estimates three evaluations cluster around the most likely horizontal offset of 7.9 ± 0.4 m. The higher scarp horizontal offset of 4.0 ± 0.5 m is derived from the first scarp offset by applying the same ratio for horizontal offsets as for vertical offsets of the two scarps (Table 2). The studied fan belongs to the light-grey generation (Qt_{2*}) whose abandonment has been dated by correlation at 5.7 ± 0.6 ^{10}Be kyr. The total strike-slip motion on the Kahnuj Fault can thus be evaluated, by addition of the contribution of the two sub-faults, to 2.3 ± 1.0 mm yr $^{-1}$ and the azimuth of displacement is around $N14 \pm 16^{\circ}E$ (Table 3).

4.5 Jiroft Fault

The Jiroft Fault represents the boundary between a mountainous zone to the west (Kuh-e-Khema, 1426 m) and the Jaz Murian depression to the east. To the south, it splits into several segments bifurcating into a southeast- then east-trending direction within the northern termination of the Makran range.

Only one site has been investigated along the Jiroft Fault (J01, $27^{\circ}35.1'N/57^{\circ}48.0'E$, Fig. 2). This site is a 'black' fan surface (Qt_{1a*} ; *cf.* the correlation fan sequence cropping out in eastern and western areas of the studied zone) made up of coarse materials (up to 1 m in diameter). Differential GPS topographic profiles yield values for the vertical offset ranging from 2.5 to 6.7 m. Nevertheless, this site is very useful for the characterization of the fault plane. Indeed, 3-D mapping of a fault plane in a case of non-horizontal topography allows estimation of both the azimuth and the dip of the fault plane, respectively at about $3^{\circ}N$ and $52^{\circ}W$.

A SPOT satellite image analysis of this fault reveals some indicators of strike-slip deformation. The offsets of fans and streams give two distinct average values: 49 ± 17 m (two measurements) for Qt_{1a} fans and 133 ± 18 m (four values) on assumed Qt_{1a*} fans (Table 4). On the basis of regional correlation, the two episodes of fan abandonment occurred, respectively, at 22.1 ± 1.6 ^{10}Be kyr and 42.0 ± 4.2 kyr. Strike-slip rates consequently range between 2.2 ± 0.8 and 3.2 ± 0.5 mm yr $^{-1}$ (Table 2). The mean strike-slip rate on the Jiroft Fault is evaluated at 2.7 ± 0.7 mm yr $^{-1}$ and the horizontal direction of motion is $N18 \pm 17^{\circ}E$ (Table 3).

4.6 Total motion accommodated through the Zagros–Makran transition zone

The sum of the fault slip rates determined through the Zagros–Makran transition zone allows us to quantify the motion of the Musandam Peninsula with respect to Jaz Murian. The Minab–Zendan–Palami fault system accommodates a convergence velocity of 5.6 ± 2.3 or 7.4 ± 2.7 mm yr $^{-1}$, in the direction $N11 \pm 24^{\circ}E$ or $N13 \pm 26^{\circ}E$, depending on the strike-slip rate considered for the Zendan Fault. Since the Minab Fault behaves like a pure thrust accommodating a $N33 \pm 53^{\circ}E$ -trending motion, a slight partitioning of minor contributions to the total convergence accommodated through the system is noted, whereas the Palami and Zendan faults are transpressional and indicate $N0^{\circ}E$ to $N5^{\circ}E$ -trending (± 7 – $19^{\circ}E$) convergence vectors. The Jiroft–Sabzevaran fault system accommodates an almost pure strike-slip motion. The horizontal velocity of its western wall with respect to its eastern wall (Jaz Murian) is 5.7 ± 1.7 mm yr $^{-1}$ in a direction $N9 \pm 12^{\circ}E$ (Table 3).

Finally we found that the total motion of the Musandam Peninsula with respect to Jaz Murian is 11.2 ± 3.9 or 13.0 ± 4.3 mm yr $^{-1}$ depending on the slip rate of the Zendan Fault, in a direction of $N11 \pm 19^{\circ}E$ and $N10 \pm 19^{\circ}E$, respectively. Along the main compressional

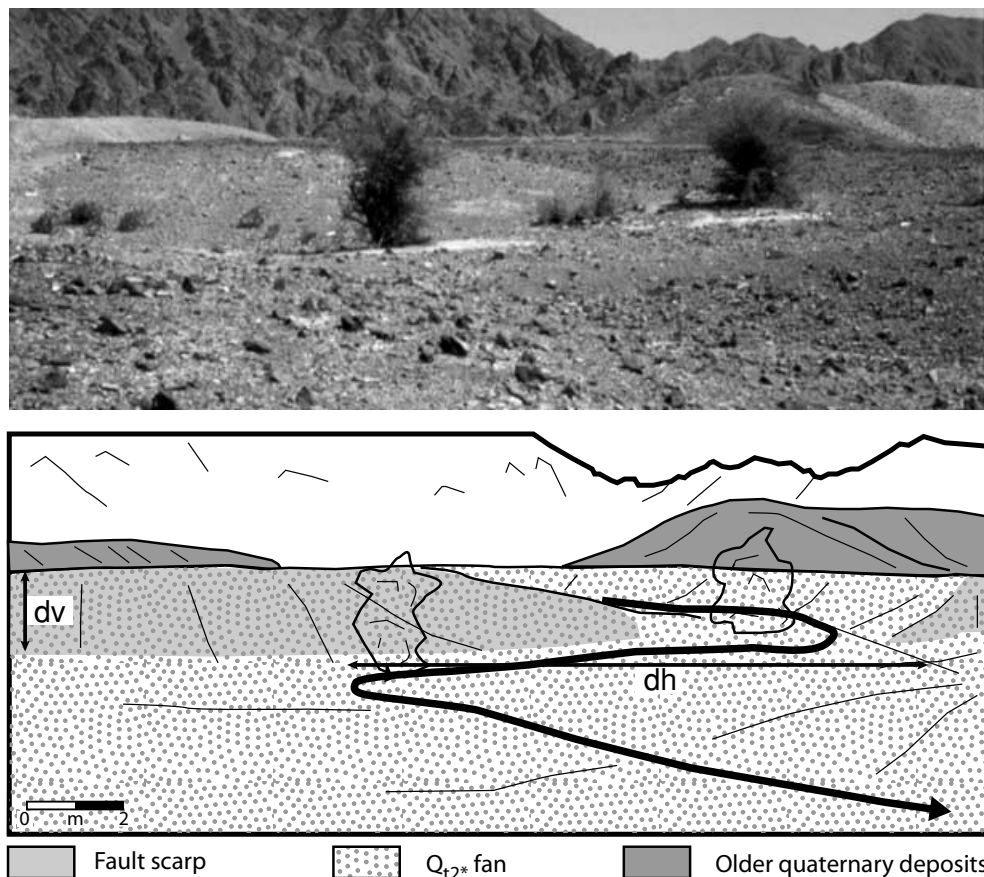


Figure 14. Frontal view of the lower scarp at site K01. The Qt_{2*} fan is offset by the fault. Vertical and horizontal offsets appear to be dv (~ 2.5 m) and dh (~ 10 m), determined by fan and stream offsets respectively. Note that at this site the Kahnuj Fault is divided into two subfaults. The upper scarp is in the background of the photograph, but is not clearly visible in this picture.

stress axis direction ($N45^{\circ}E$), this corresponds to a displacement rate of 9.5 ± 3.5 or 11.2 ± 3.9 mm yr^{-1} , respectively (Table 3).

5 DISCUSSION

The Minab–Zendan fault zone accommodates the transition between the Iranian collision zones and the Makran accretionary prism of subduction. The fault zone itself is made up of two main fault systems. The first one is the Minab–Zendan fault system, consisting of three more or less parallel faults (Minab, Zendan, and Palami), whose mean trend is $N160^{\circ}E$. The second one includes two major north-trending faults, the Sabzevaran and Jiroft faults and a secondary fault, the Kahnuj Fault. Fault segmentation and kinematics are consistent with a transpressional regime produced by a roughly northeast-trending compressional stress regime. Combined geomorphic arguments and topographic levelling with stratigraphic and radiometric dating presented here also constrain the slip rate of the fault system. In particular, we present here a new chronological chart for the Quaternary deposits of the study area.

Dufaure *et al.* (1978) (see also Dufaure 1984) first established that the Minab area, located in the western part of the studied zone, is characterized by Quaternary alluvial deposits stratigraphically organized in a four-level sequence. The first deposit of the Dufaure *et al.* (1978) classification (Qt_{2a}) is an alluvial terrace dated between 5 and 9 kyr BP. According to our study, the second level (Qt_2) corresponds to terraces or fan surfaces assigned to the epi-Palaeolithic,

from the industries they display, and dated at 13.6 ± 1.1 ^{10}Be kyr. In the Minab area, the third level of the Dufaure *et al.* (1978) classification (Qt_{1a}) displays Mousterian industries (100–50 kyr BP). ^{10}Be exposure ages performed on geomorphologically related fans near the Sabzevaran Fault yield to two distinct deposition events at 22.1 ± 1.6 ^{10}Be kyr, and 42 ± 4.2 kyr (respectively Qt_{1a} and Qt_{1as}). Finally, accordingly to the industries it displays, the highest level of the Dufaure *et al.* (1978) classification (Qt_1) is assigned to the Late Acheulian age (300–100 kyr BP). However, there may be depositional gaps in the Minab area where Dufaure (1984) established their classification, and this highest level may correspond to one of the deposition stages described in the literature for that time interval, that is at around 65–70, 80, 115–120, 180–210 or 300–325 kyr BP.

The lateral and vertical offsets affecting the Quaternary alluvial fans and terraces has been estimated by topographic profiles established using differential GPS receivers, as well as analysis of aerial photographs and satellite images. We obtain horizontal fault slip velocities that range from 0.4 to 3.0 mm yr^{-1} for individual faults (or 4.2 mm yr^{-1} due to an uncertainty linked to the slip of the Zendan Fault). The similarity of convergence directions through the fault zones of the study area (about $N10^{\circ}E$) confirms that there is no partitioning. The total motion accommodated between the Hormoz Strait and the Jaz Murian depression is 11.2 ± 3.9 or 13.0 ± 4.3 mm yr^{-1} in a direction trending about $N10^{\circ}E$ (Fig. 15). The convergence direction is consistent with the NUVEL-1 convergence direction and

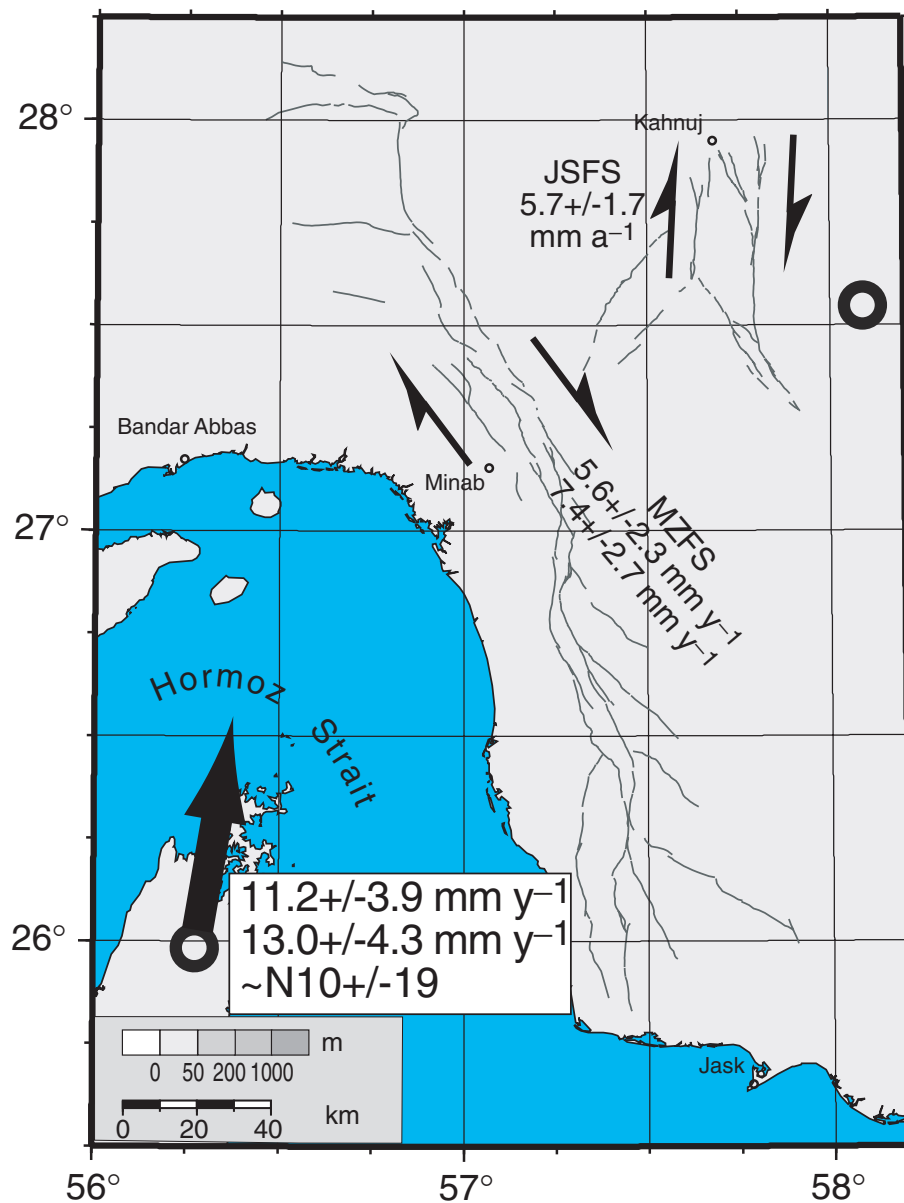


Figure 15. Tectonic motion through the transition Zagros–Makran. The active faults traces are mapped after Regard *et al.* (2004). Two fault systems accommodate the motion: the Minab–Zendan fault system (MZFS) and the Jiroft–Sabzevaran fault system (ZJFS). The strike-slip component accommodated by both of them is indicated. Their sum indicate a convergence vector of Munsandam (black arrow) relatively to Jaz Murian (black open circle) of about 12 mm yr^{-1} directed $\sim\text{N}10^\circ\text{E}$.

earthquake focal mechanism inversion (Regard 2003). The velocity is consistent with GPS results of about 10 mm yr^{-1} , from the local network (Bayer *et al.* 2005), and about 11 mm yr^{-1} from the regional network (Nilforoushan *et al.* 2003; Vernant *et al.* 2004). In addition, the current study indicates that the parts accommodated by the two fault systems constituting the Zagros–Makran transfer zone are roughly equivalent. The Minab–Zendan fault system accommodates 5.6 ± 2.3 or $7.4 \pm 2.7 \text{ mm yr}^{-1}$ in a direction trending about $\text{N}12^\circ\text{E}$ while the Jiroft–Sabzevaran fault system accommodates $5.7 \pm 1.7 \text{ mm yr}^{-1}$ in a direction $\text{N}9 \pm 12^\circ\text{E}$ (Fig. 15). However, on a larger scale, the two fault systems may not play the same role in the accommodation of Arabian–Eurasian convergence. Indeed, to the north, the Minab–Zendan fault system connects to the Zagros through the MZT, to which it is directly linked, whereas the Jiroft–Sabzevaran fault system goes northwards within the

Nayband–Gowk fault system, to finally transfer the deformation to the northern Iranian compressional ranges (Kopet-Dagh, Alborz, Apsheron) (*cf.* Fig. 1).

This study documents different faults which all make a significant contribution to the total convergence accommodated through the system. This is not supported by GPS data which are not dense enough to discriminate the respective role of each fault (Bayer *et al.* 2005). This discrepancy contrasts with the far-field similarity of the results of this study and GPS studies. This could be explained by considering the deep geometry of the faults. Indeed they may all connect at depth to make a single crustal-scale or lithospheric-scale structure. At the surface the convergence accommodated through this deep structure could be distributed in space and/or time through the different faults. In other words, deformation could occur on one single structure at a given time but the deformation could shift

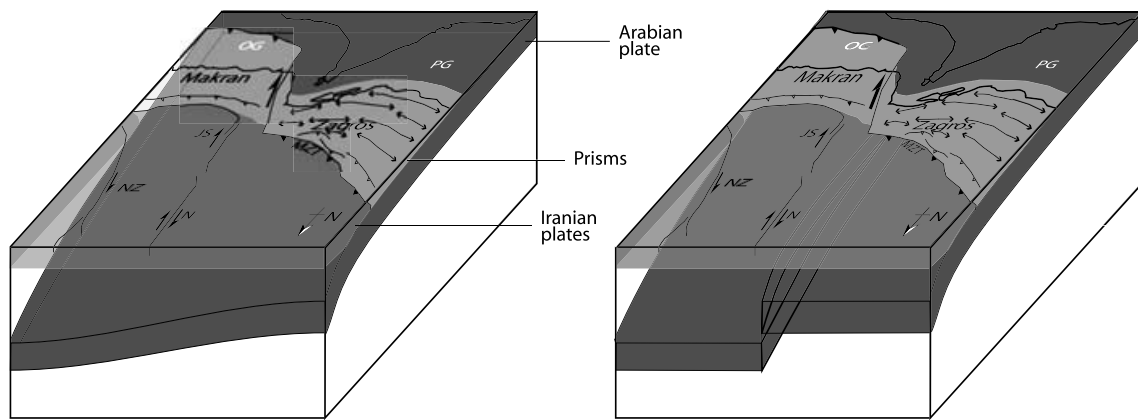


Figure 16. Schematic diagrams showing two different possible geometries for the slab under the Zagros–Makran transition zone: the slab can be continuous with some bend (right) or in two independent parts (left). PG, Persian Gulf; OG, Gulf of Oman; N, Nayband Fault; JS, Jiroft and Sabzevaran faults; NZ, Neh and Zahedan faults.

periodically to another structure. In this scheme GPS give an instantaneous image of actual deformation whereas the long-term geological rate shows an integrated deformation pattern over thousands of years. Further studies may check this hypothesis and its mechanical implications, and possibly give a characteristic time for the flip of deformation between the different structures.

Further east, the transition zone between the Arabian–Eurasian collision zone and the Makran subduction zone appears wider (Regard *et al.* 2004). The results presented here confirm this previous observation, since the study area accommodates only one-third to one-half of the total differential motion expected between Zagros and Makran (compare the Arabian–Eurasian convergence estimates from this study of $\sim 12 \text{ mm yr}^{-1}$ with the $23\text{--}35 \text{ mm yr}^{-1}$ estimates from other studies). This motion discrepancy must thus be accommodated by other structures in the east Makran, close to the East Iranian Ranges, as indicated by geological studies (Tirrul *et al.* 1983; Byrne *et al.* 1992; Walker & Jackson 2002), and by GPS results (Vernant *et al.* 2004; Bayer *et al.* 2005). These structures transfer the deformation northwards, as the Jiroft–Sabzevaran–Nayband–Gowk system does. This distribution of deformation on different north-trending fault zones suggests a continuity of Zagros- and Makran-related structures and processes from west to east that could be related to a flexure in the shape of the slab, from that under the Zagros collision zone to that within the Makran subduction zone (*cf.* Fig. 16). Analogue modelling shows that such wide deformation zones imply relatively low deformation of the slab at depth (Regard *et al.* 2005). In addition the width of this transition zone may be influenced, in experiment as in the Zagros–Makran case, by the presence of inherited lithospheric-scale zones of weakness, such as the former plate boundaries of the Lut Block. This widely distributed deformation characterizes an immature transform zone, since under mature conditions collision would involve slab break off at depth which would individualize two different slabs, respectively under the subduction zone and under the collision, which would lead to individualization of a superficial fault zone, finally turning into a transform fault zone.

It is interesting to note that the eastern termination of the Makran is also characterized by a subduction–collision transfer zone. The transfer zone constitutes the Chaman, Ghazaband and Ornach–Nal faults. The system connects the Makran accretionary prism to the Pamirs (Panjshir Fault) (Lawrence *et al.* 1992). It is made up of three main faults (*cf.* Fig. 17):

(1) The 860 km long Chaman Fault connecting the Panjshir Fault to the north to the inner Makran thrusts to the south. Its azimuth is $N10^\circ E$ to $N35^\circ E$, and it is slightly oblique to the convergence vector, lying between $N0^\circ E$ and $N10^\circ E$, after the NUVEL-1 model (DeMets *et al.* 1990). The Chaman Fault is active and 60 per cent of its trace cuts Quaternary formations.

(2) The Quetta line–Ghazaband Fault, which laterally passes to a thrust fault at the edge of the Katawaz Basin.

(3) The 270 km-long Ornach–Nal Fault which displays evidence of activity to the north and seems to end to the south under sand deposits.

The overall system is thought to accommodate between 25 and 35 mm yr^{-1} , following geological evidence (Beun *et al.* 1979), and 40 mm yr^{-1} , after the NUVEL-1 model (DeMets *et al.* 1990).

There is a strong analogy between the Chaman fault system and the Zagros–Makran transition zone. The two systems are made of *en echelon* faults and accommodate oblique convergence through transpressional faults. The most important part of the deformation is transmitted to the inner Makran and there is no evidence of active deformation transmission to the frontal, offshore, Makran thrust. Conversely the Chaman system differs from the Zagros–Makran transition by a larger localization of the deformation and some slight evidence of partitioning to the north between the Chaman strike-slip fault and the Sulaiman fold belt (Lawrence *et al.* 1992; Davis & Lillie 1994). The Chaman fault system is moreover characterized by longer fault segments and an azimuth closer to the convergence vector. In summary, the modern pattern of the Zagros–Makran transition zone and the Chaman fault system express the same mechanism. They only differ in age: the Zagros–Makran fault system is young (it must be younger than 5 Myr) whereas the Chaman fault system is mature, at least 20–25 Myr old, and shows evidence of cumulative offsets ($\sim 450 \text{ km}$) (Lawrence *et al.* 1992). The maturity of the Chaman system is attested to by the localization of the active deformation. On the contrary the Zagros–Makran transition zone efficiently decouples its eastern and western walls, implying no connection at depth like a continuous slab (see above and Regard *et al.* 2005).

Comparison between the Chaman fault system and the Zagros–Makran transition zone shows evidence of slip on the inner Makran thrust and not on the frontal one. There is, however, current debate on where deformation occurs in accretionary prisms (Gutscher

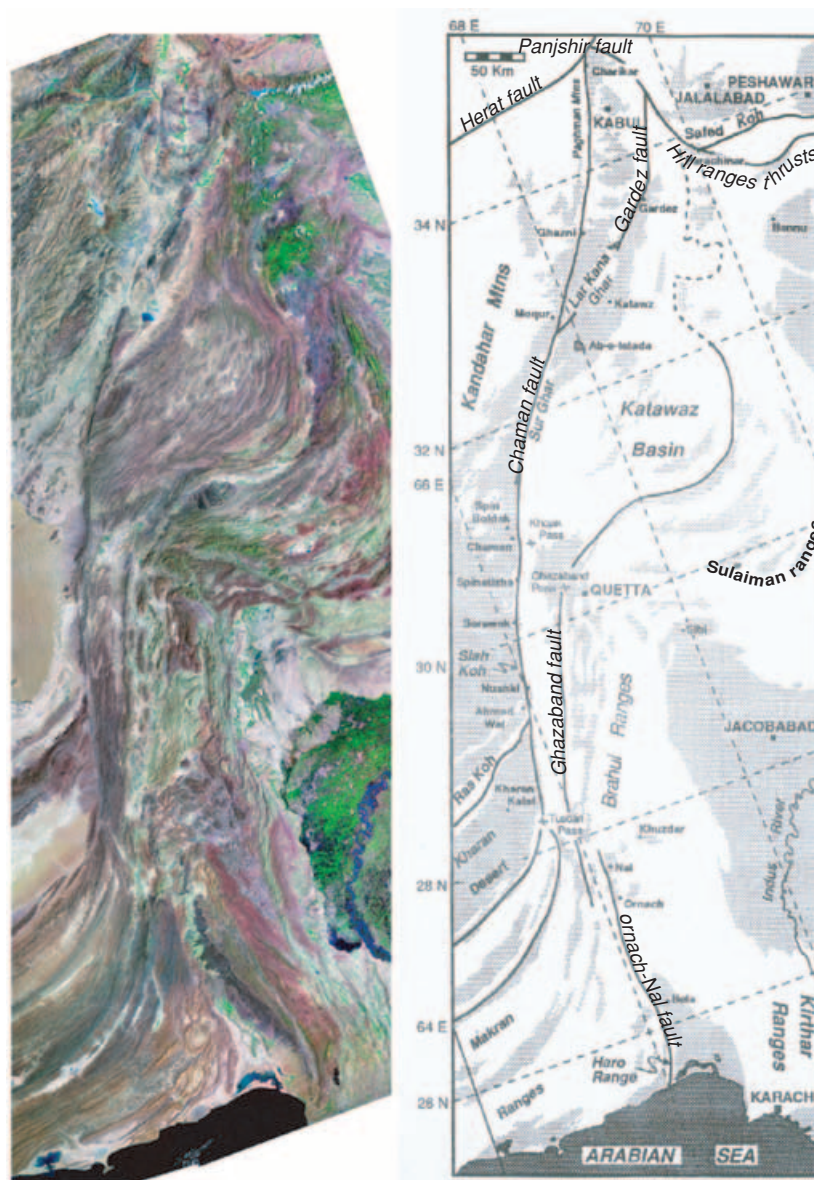


Figure 17. Landsat image of the Chaman Fault (bands 7, 4 and 2) and its tectonic interpretation, after Lawrence *et al.* (1992).

et al. 1998). Actually our results show that there is no detectable Quaternary activity of the frontal thrust of the Makran at its eastern and western termination. During the Quaternary, most of the deformation should occur within the inner, onshore, Makran thrusts, which supports the episodic model for accretion, i.e. the episodic flip of deformation from an inner wedge to its front and vice versa (e.g. Gutscher *et al.* 1998).

6 CONCLUSIONS

The transition between the Iranian collision zone and the Makran subduction zone in southeastern Iran is characterized by two distinct fault systems. The first, the Minab–Zendan–Palami fault system, connects the Zagros continental prism to the Makran. It trends NNW–SSE and accommodates about 6 mm yr^{-1} of convergence in a direction about $\text{N}10^\circ\text{E}$. The second, the Jiroft–Sabzevaran fault system, connects the Makran to the deforming belt in northern Iran (Alborz and Kopet-Dagh). It trends north–south and also accom-

modates about 6 mm of convergence in a direction about $\text{N}10^\circ\text{E}$. The contribution of this system is about 12 mm yr^{-1} in a direction $\text{N}10^\circ\text{E}$. It is noteworthy that instead of a good coherence with the $\text{N}06^\circ\text{E}$ direction of the convergence vector deduced by global GPS, the convergence rate accommodated here is far from the 24 mm yr^{-1} accommodated between Arabia and Eurasia (see table 1 in Regard *et al.* (2004) which is based on the work of Sella *et al.* (2002)). The ‘missing’ convergence must be found farther east, along the north-trending East Iranian ranges (Vernant *et al.* 2004).

ACKNOWLEDGMENTS

This work is part of the cooperative research agreement between the INSU-CNRS (France) and International Institute of Earthquake Engineering and Seismology (IIEES, Iran), supervised by D. Hatzfeld and M. G. Ashtyani. We thank IIEES for fieldwork assistance and M. Mokhtari for support and administrative assistance. Funding was provided by the Intérieur de la Terre programme (IT, INSU-CNRS)

and the IIEES within the above mentioned cooperative agreement. The preliminary reconnaissance field work around the Minab area was done with J. Mercier and consequently we have benefited from the observations that he made 20 years ago with J.-J. Dufaure, C. Thibault and M. H. Kadjar. We thank J. Collina-Girard and G. Dollfus for their help in reassessing the pre-historic periods described by C. Thibault. SPOT images were provided thanks to the ISIS programme support (CNES). We thank the STSI team (Cerege) for computational facilities, F. Michel for its preliminary work, D. Chardon, C. Faccenna and J. Martinod for revisions of an early version of the manuscript and R. Bayer and D. Hatzfeld for helpful discussions. Useful comments from R. Walker and G. d'Addezio helped improve this manuscript.

REFERENCES

- Alavi, M., 1994. Tectonics of the Zagros orogenic belt of Iran: new data and interpretations, *Tectonophysics*, **229**, 211–238.
- Avouac, J.-P., 1993. Analysis of scarp profiles: evaluation of errors in morphologic dating, *J. geophys. Res.*, **98**, 6745–6754.
- Bar-Matthews, M. & Ayalon, A., 2005. Speleothems as paleoclimate indicators, a case study from Soreq Cave located in the eastern Mediterranean Region, Israel, in *Past Climate through Europe and Africa: Developments in Paleoenvironmental Research*, eds Battarbee, R.W., Gasse, F. & Stickley, C.E., Springer.
- Bar-Matthews, M., Ayalon, A. & Kaufman, A., 1997. Late Quaternary Paleoclimate in the eastern Mediterranean region from stable isotope analysis of speleothems at Soreq Cave, Israel, *Quaternary Res.*, **47**, 155–168.
- Bayer, R. *et al.*, 2003. Active deformation in the Zagros–Makran transition zone inferred from GPS measurements in the interval 2000–2002 (abstract EGS 2003), *Geophys. Res. Abstr.*, **5**, 05891.
- Bayer, R. *et al.*, 2005. Active deformation in Zagros–Makran transition zone inferred from GPS measurements, *Geophys. J. Int.*, submitted.
- Berberian, M. & King, G.C.P., 1981. Towards a paleogeography and tectonic evolution of Iran, *Can. J. Earth Sci.*, **18**, 210–265.
- Beun, N., Border, P. & Carbonnel, J., 1979. Premières données quantitatives relatives au coulisage du décrochement de Chaman (Afghanistan du sud-est), *C. R. Acad. Sci. Paris*, **288D**, 931–934.
- Blanc, E.J.-P., Allen, M.B., Inger, S. & Hassani, H., 2003. Structural styles in the Zagros simple folded zone, Iran, *J. Geol. Soc. Lond.*, **160**, 401–412.
- Braucher, R. *et al.*, 2000. Application of in situ-produced cosmogenic ^{10}Be and ^{26}Al to the study of lateritic soil development in tropical forest: Theory and examples from Cameroon and Gabon, *Chemical Geology*, **170**, 95–111.
- Brown, E.T., Bourlès, D.L., Colin, F., Sanfo, Z., Raisbeck, G.M. & Yiou, F., 1991. Examination of surface exposure ages of Antarctic moraines using in-situ produced ^{10}Be and ^{26}Al , *Geochim. Cosmochim. Acta*, **55**, 2269–2283.
- Burns, S.J., Matter, A., Franck, N. & Mangini, A., 1998. Speleothem-based paleoclimate record from northern Oman, *Geology*, **26**(6), 499–502.
- Burns, S.J., Fleitman, D., Matter, A., Neff, U. & Mangini, A., 2001. Speleothem evidence from Oman for continental pluvial events during interglacial periods, *Geology*, **29**(7), 623–626.
- Byrne, D.E., Sykes, L.R. & Davis, D.M., 1992. Great thrust earthquakes and aseismic slip along the plate boundary of the Makran subduction zone, *J. geophys. Res.*, **97**(B1), 449–478.
- Carretier, S., Ritz, J.-F., Jackson, J. & Bayasgalan, A., 2002. Morphological dating of cumulative reverse fault scarps: examples from the Gurvan Bogd fault system, Mongolia, *Geophys. J. Int.*, **148**, 256–277.
- Cerling, T.E. & Craig, H., 1994. Geomorphology and in-situ cosmogenic isotopes, *Ann. Rev. Earth Planet. Sci.*, **22**, 273–317.
- Clark, I.D. & Fontes, J.C., 1990. Paleoclimatic reconstruction in northern Oman based on carbonates from hyperalkaline groundwaters, *Quaternary Res.*, **33**, 320–336.
- CMT, 2002. *Harvard University Moment Tensor catalog (CMT Project)*, online data set: <http://www.seismology.harvard.edu/projects/CMT/>
- Davis, D.M. & Lillie, R.J., 1994. Changing mechanical response during continental collision: active examples from the foreland thrust belts of Pakistan, *J. Struct. Geol.*, **16**, 21–34.
- DeMets, C., Gordon, R.G., Argus, D.F. & Stein, S., 1990. Current plate motions, *Geophys. J. Int.*, **101**, 425–478.
- Dufaure, J.-J., 1984. Piémont et transversale: Le contact Makran-Zagros (Iran du Sud), in *Montagnes et Piémonts: Actes du Colloque de géomorphologie*, pp. 423–426, Rev. Geogr. Des Pyrénées et du Sud-Ouest, Toulouse, France.
- Dufaure, J.J., Thibault, C., Kadjar, M.H. & Mercier, J.L., 1978. La zone de failles du Zendan (Iran du Sud-Est): I—Géomorphologie et Stratigraphie du Quaternaire, paper presented at *Réunion Annuelle des Sciences de la Terre (6th RAST)*, Soc. Géol. De Fr., Orsay, France.
- Dziewonski, A.M., Chou, T.-A. & Woodhouse, J.H., 1981. Determination of earthquake source parameters from waveform data studies of global and regional seismicity, *J. geophys. Res.*, **86**, 2825–2852.
- Farhodi, G., 1978. A comparison of Zagros geology to island arcs, *J. Geol.*, **86**, 323–334.
- Faure-Muret, A. & Choubert, G., 1971. Aperçu de l'évolution structurale de l'Iran, *Tectonique de l'Afrique*, Sciences de la Terre, Vol. 6, pp. 141–151, Unesco, Paris, France.
- Fontugne, M., Kuzucuoglu, C., Karabiyikoglu, M., Hatte, C. & Pastre, J.-F., 1999. From Pleniglacial to Holocene: a ^{14}C chronostratigraphy of environmental changes in the Konya Plain Turkey, *Quaternary Sci. Rev.*, **18**, 573–591.
- Freund, R., 1970. Rotation of strike-slip faults in Sistan, southeast Iran, *J. Geol.*, **78**, 188–200.
- Fruehn, J., White, R.S. & Minshull, T.A., 1997. Internal deformation and compaction of the Makran accretionary wedge, *TerraNova*, **9**, 101–104.
- Garzanti, E., Critelli, S. & Ingersoll, R.V., 1996. Paleogeographic and paleotectonic evolution of the Himalayan range as reflected by detrital modes of Tertiary sandstones and modern sands (Indus transect, India and Pakistan), *Bull. geol. Soc. Am.*, **108**, 631–642.
- Gaudemer, Y., Tapponnier, P. & Turcotte, D.L., 1989. River offsets across active strike-slip faults, *Ann. Tecton.*, **3**, 55–76.
- Gaudemer, Y. *et al.*, 1995. Partitioning of crustal slip between linked, active faults in the eastern Qilian Shan, and evidence for a major seismic gap, the 'Tianzhu gap', on the western Haiyuan Fault, Gansu (China), *Geophys. J. Int.*, **120**, 599–645.
- Glennie, K.W. & Singhvi, A.K., 2002. Event stratigraphy, paleoenvironment and chronology of SE Arabian deserts, *Quaternary Sci. Rev.*, **21**, 853–869.
- Gutscher, M.A., Kukowski, N., Malavieille, J. & Lallemand, S., 1998. Episodic imbricate thrusting and underthrusting: analog experiments and mechanical analysis applied to the Alaskan accretionary wedge, *J. geophys. Res.*, **103**, 10 161–10 176.
- Harms, J.C., Cappel, H.N. & Francis, D.C., 1984. The Makran coast of Pakistan: its stratigraphy and hydrocarbon potential, in *Marine Geology and Oceanography of the Arabian Sea and Coastal Pakistan*, pp. 3–26, eds Haq, B.U. & Milliman, J.D., Van Nostrand Reinhold, New York.
- Hoelzmann, P., Gasse, F., Dupont, L.M., Salzmann, U., Staubwasser, M., Leuschner, D.C. & Sirocko, F., 2005. Palaeoenvironmental changes in the arid and sub arid belt (Sahara-Sahel-Arabian Peninsula) from 150 kyr to present, in *Past Climate Variability Through Europe and Africa, Developments in Paleoenvironmental Research*, eds Battarbee, R.W., Gasse, F. & Stickley, C.E., Springer.
- Jackson, J., Haines, J. & Holt, W., 1995. The accommodation of Arabia–Eurasia plate convergence in Iran, *J. geophys. Res.*, **100**(B8), 15 205–15 219.
- Jackson, J.A., Priestley, K., Allen, M. & Berberian, M., 2002. Active tectonics of the South Caspian Basin, *Geophys. J. Int.*, **148**, 214–245.
- Kadinsky-Cade, K. & Barazangi, M., 1982. Seismotectonics of southern Iran: the Oman line, *Tectonics*, **1**(5), 389–412.
- Kopp, C., Fruehn, J., Flueh, E.R., Reichert, C., Kukowski, N., Bialas, J. & Klaeschen, D., 2000. Structure of the Makran subduction zone

- from wide angle and reflection seismic data, *Tectonophysics*, **329**, 171–191.
- Lal, D., 1991. Cosmic ray labeling of erosion surfaces: *in-situ* nuclide production rates and erosion models, *Earth planet. Sci. Lett.*, **104**, 424–439.
- Lawrence, R.D., Khan, S.H. & Nakata, T., 1992. Chaman Fault, Pakistan-Afghanistan, *Ann. Tecton.*, **VI**, Special Issue Suppl., 196–223.
- McCall, G.J.H., 1997. The geotectonic history of the Makran and adjacent areas of southern Iran, *J. Asian Earth Sci.*, **15**(6), 517–531.
- McCall, G.J.H. & Kidd, R.G.W., 1982. The Makran, southeastern Iran: the anatomy of a convergent plate margin active from Cretaceous to present, in *Trench-forearc Geology: Sedimentation and Tectonics on Modern and Ancient Active Plate Margins*, Geological Society of London Special Publication 10, pp. 387–397, ed. Leggett, J.K., Blackwell Scientific, Oxford.
- McCall, G.J.H. et al., 1985. *Minab Quadrangle Map 1:250,000 and Explanatory Text*, Geological Survey of Iran.
- McClusky, S.M., Reillinger, R., Mahmoud, S., Ben Sari, D. & Tealeb, A., 2003. GPS constraints on Africa (Nubia) and Arabia plate motions, *Geophys. J. Int.*, **155**, 126–138.
- NEIC, 2002. *USGS National Earthquake Information Center Catalog Online Data Set*, <http://neic.usgs.gov/>
- Nilforoushan, F. et al., 2003. GPS network monitors the Arabia-Eurasia collision deformation in Iran, *J. Geod.*, **77**, 411–422.
- Regard, V., 2003. Lateral and temporal evolution from subduction to collision: insights from Iranian tectonics (Zagros-Makran) and physical modeling (in French and English), *Thesis*, Université Aix-Marseille III (available at: <http://tel.ccsd.cnrs.fr/documents/archives0/00/00/37/77/index.html>).
- Regard, V., Bellier, O., Thomas, J.-C., Abbassi, M.R., Mercier, J., Shabanian, E., Fegghi, K. & Soleymani, S., 2004. The accommodation of Arabia-Eurasia convergence in the Zagros-Makran transfer zone, SE Iran: a transition between collision and subduction through a young deforming system, *Tectonics*, **23**, TC4007, doi:10.1029/2003TC001599.
- Regard, V., Faccenna, C., Martinod, J. & Bellier, O., 2005. Slab pull and indentation tectonics: insights from 3D laboratory experiments, *Phys. Earth planet. Int.*, **149**, 99–113.
- Sanlaville, P., 1992. Changements climatiques dans la péninsule Arabique durant le Pléistocène supérieur et l'Holocène, *Paléorient*, **18**(1), 5–26.
- Schumm, S.A., Mosley, M.P. & Weaver, W.E., 1987. *Experimental Fluvial Geomorphology*, John Wiley, New York.
- Sella, G.F., Dixon, T.H. & Mao, A., 2002. REVEL: a model for Recent plate velocities from space geodesy, *J. geophys. Res.*, **107**, doi:10.1029/2000JB000033.
- Siame, L.L. et al., 1997. Cosmogenic datings of alluvial fans along the Central Andes El Tigre Fault (Argentina): paleoclimatic and tectonic implications, *Geology*, **25**, 975–978.
- Siame, L.L., Braucher, R., Bourlès, D.L., Bellier, O. & Sébrier, M., 2001. Cosmic ray exposure dating of geomorphic surface features using *in situ* production of Be-10: tectonic and climatic implications, *Bull. Soc. Géol. Fr.*, **172**, 223–236.
- Talebian, M. & Jackson, J., 2002. Offset on the main Recent fault of NW Iran and implications for the late Cenozoic tectonics of the Arabia-Eurasia collision zone, *Geophys. J. Int.*, **150**, 422–439.
- Tatar, M., Hatzfeld, D., Martinod, J., Walpersdorf, A., Ghafori-Ashtiany, M. & Chery, J., 2002. The present-day deformation of the central Zagros from GPS measurements, *Geophys. Res. Lett.*, **29**(19), doi: 10.1029/2002GL015427.
- Tirrul, R., Bell, I.R., Griffith, R.J. & Camp, V.E., 1983. The Sistan suture zone of eastern Iran, *Geol. soc. Am. Bull.*, **94**, 134–150.
- Vernant, P. et al., 2004. Contemporary crustal deformation and plate kinematics in the Middle East constrained by GPS measurements in Iran and Northern Oman, *Geophys. J. Int.*, **157**, 381–398.
- Walker, R. & Jackson, J., 2002. Offset and evolution of the Gowk fault, SE Iran; a major intra-continental strike-slip system, *J. Struct. Geol.*, **24**, 1677–1698.
- Wessel, P. & Smith, W.H.F., 1995. New version of the generic mapping tools released, *EOS, Trans. Am. geophys. Un.*, **76**, 329.
- White, R.S., 1982. Deformation of the Makran accretionary sediment prism

in the Gulf of Oman (north-west Indian Ocean), in *Trench-forearc Geology: Sedimentation and Tectonics on Modern and Ancient Active Plate Margins*, ed. Leggett, J.K., *Geol. Soc. Spec. Publ.*, **10**, 69–84 Blackwell Scientific, Oxford.

Yan, Z. & Petit-Maire, N., 1994. The last 140 ka in the Afro-Asian arid/semi-arid transitional zone, *Palaeogeog. Palaeoclim. Palaeoecol.*, **110**, 217–233.

APPENDIX A: OFFSET DETERMINATION

A horizontal offset (dss) can be deduced from knowledge of the vertical offset (dv) together with that of the dip of the fault plane (δ) and the pitch of its striae (γ) (see Fig. A1). We use intermediate values of the total displacement on the fault plane (s), the dip-slip displacement (dvs) and their respective horizontal projections (dh and dd) (Fig. A1). Triangular relations give:

$$dd = \frac{dv}{\tan \theta} \quad (\text{A1})$$

and also $dd^2 + dss^2 = dh^2$ and $dh^2 + dv^2 = s^2$. Therefore:

$$s^2 = dss^2 + dd^2 + dv^2 \quad (\text{A2})$$

thus

$$dss^2 = s^2 - dv^2 \left(1 + \frac{1}{\tan^2 \delta} \right). \quad (\text{A3})$$

Triangular relations also give:

$$\frac{dvs}{s} = \sin \gamma \quad (\text{A4})$$

then $dss^2 + dvs^2 = s^2$ gives

$$dss^2 = s^2 \cos^2 \gamma. \quad (\text{A5})$$

When incorporating (A5) in (A3) we obtain a relation that links the pitch (γ), the vertical offset (dv), the horizontal offset (dss) and the dip of the fault plane (δ):

$$dss = \frac{dv}{\tan \gamma} \sqrt{1 + \frac{1}{\tan^2 \delta}}. \quad (\text{A6})$$

An important item of information for seismic hazard is the finite slip along the fault plane. In Fig. A1 it is represented by s , whose relationships with dss or dv are formulated by eq. (A3).

APPENDIX B: DISPLACEMENT ACROSS THE FAULT EXPRESSED IN NORTH AND EAST MOTION

For the geodynamic conclusions it is important to deduce a velocity of the southwestern part of the study zone with respect to the northeastern one. We aim to give this in north, east and vertical components (respectively, vN , vE and vv). They are easily derived from the offsets in the same directions (respectively, dN , dE and dv) and deduced from Az and α , respectively, the azimuth of the fault plane counted clockwise from the north ($N0^\circ E$ to $N360^\circ E$) and the angle between the azimuth of the plane and the horizontal convergence vector. $\alpha + Az$ represents the azimuth of the convergence vector through the fault. Thus, after the relations of Appendix A, it is possible to calculate (Fig. A1):

$$dN = dh \cos(\alpha + Az) \quad (\text{B1})$$

$$dE = dh \sin(\alpha + Az) \quad (\text{B2})$$

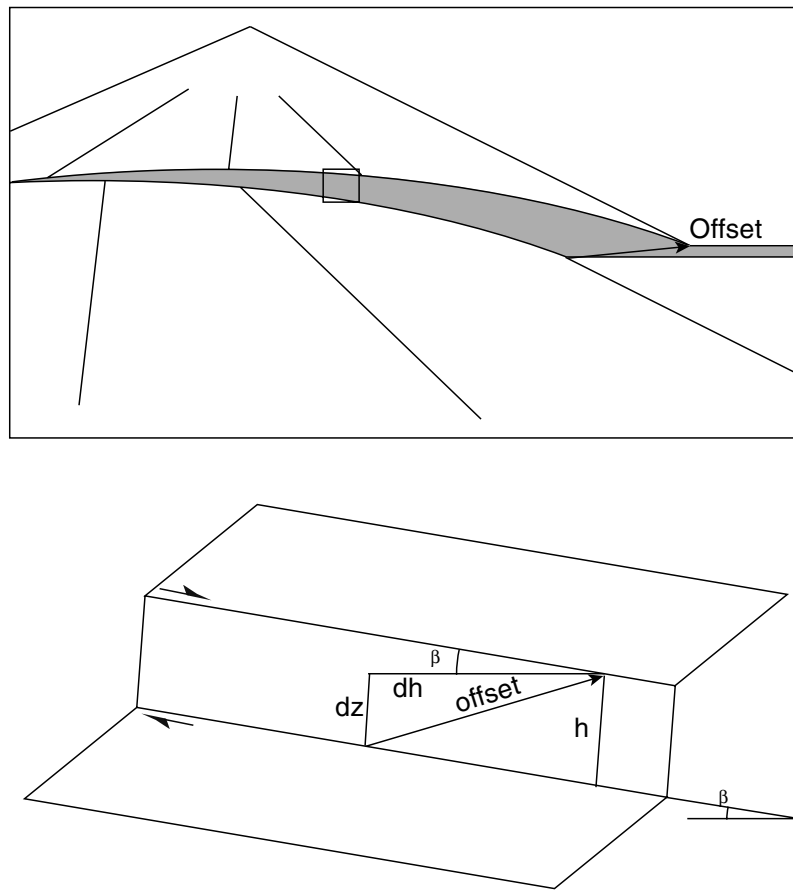


Figure C1. Calculation of offsets where the slope parallel to the fault is non-zero (β here). Top: schematic case of offset measurements on the fan side. Bottom: enlargement at fault scarplet. Unlike in the top view, the assumption is made that the scarp is locally rectangular, the observation window being small enough. The observed vertical offset is h , together with the knowledge of the horizontal offset dh , leads to the calculation of a true vertical offset dz .

Table D1. Table of offset estimates. See text for details.

Profile	Quality	Offset	Offset high	Offset low	Offset mean
D-A			5.0	3.6	4.3
D-B		2.94			
F	Bad		3.6	1.7	2.6
H	Good		2.03	1.85	1.94
J	Very good	2.36			
L	?	0.73			
N	Good	1.74			
P			2.03	1.23	1.63
R1		2.24			
R2			2.24		

Mean offset	N	Std	Std (%)	Conf. 66%
1.98	7	0.30	15.16	0.108

Site M07

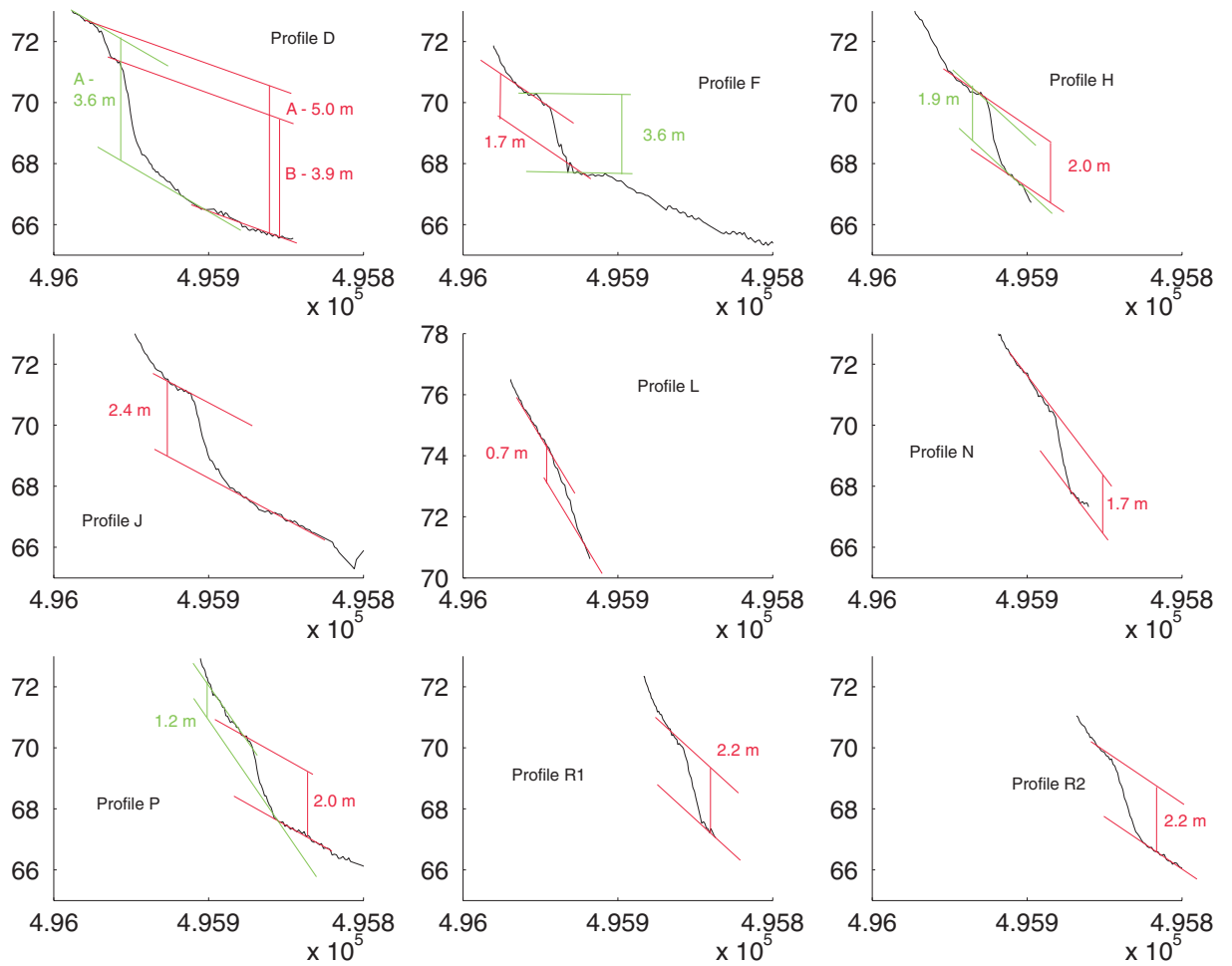


Figure D1. Profiles across the fault. The abscissa is north–south with coordinates in metres in the UTM 40 North reference frame. The ordinate is the elevation, indicated in metres above sea level. Vertical offset evaluations are in red and green, based on the vertical distance between two parallel lines, representing, respectively upstream and downstream topographic fan envelopes.